Diurnal Warm Layers in the ocean: Energetics, non-dimensional scaling, and parameterization

M. Schmitt,[1] H. T. Pham,[2] S. Sarkar,[2,3] K. Klingbeil,[1] and L. Umlauf[1]

[1] *Leibniz-Institute for Baltic Sea Research, Warnemünde, Germany*

[2] *Mechanical and Aerospace Engineering, University of California at San Diego, USA*

[3] *Scripps Institution of Oceanography, University of California at San Diego, USA*

Corresponding author: Mira Schmitt, mira.schmitt@io-warnemuende.de

ABSTRACT: Diurnal Warm Layers (DWLs) form near the surface of the ocean on days with strong solar radiation, weak to moderate winds, and small surface-wave effects. Here, we use idealized second-moment turbulence modelling, validated with Large Eddy Simulations (LES), to study the properties, dynamics and energetics of DWLs across the entire physically relevant parameter space. Both types of models include representations of Langmuir turbulence (LT). We find that LT only slightly modifies DWL thicknesses and other bulk parameters under equilibrium wave conditions, but leads to a strong reduction in surface temperature and velocity with possible implications for air-sea coupling. Comparing tropical and the less frequently studied high-latitude DWLs, we find that LT has a strong impact on the energy budget and that rotation at high latitudes strongly modifies the DWL energetics, suppressing net energy turnover and entrainment. We identify the key non-dimensional parameters for DWL evolution and find that the scaling relations of Price et al. (1986) provide a reliable representation of the DWL bulk properties across a wide parameter space, including high-latitude DWLs. We present different sets of revised model coefficients that include the deepening of the DWL due to LT and other aspects of our more advanced turbulence model to describe DWL properties at midday and during the DWL temperature peak in the afternoon, which we find to occur around 15:00-16:30 for a broad range of parameters.

1. Introduction

Diurnal Warm Layers (DWLs) form near the surface of the ocean on days with strong solar radiation, weak to moderate winds, and weak surface-wave activity. Reviewing existing literature, Kawai and Wada (2007) noted that DWLs are a wide-spread feature, found at all latitudes and characterized by typical sea-surface temperature (SST) anomalies of $\mathcal{O}(0.1-1)$ °C and typical thicknesses of $\mathcal{O}(1-10)$ m. DWLs isolate the deeper parts of the surface layer from atmospheric forcing (Wijesekera et al. 2020), provide a niche for marine microorganisms (Kahru et al. 1993), modify air-sea fluxes (Matthews et al. 2014), and feed back to the atmosphere in ways that are just beginning to be understood (Brilouet et al. 2021).

Recent field investigations with specialized instrumentation (Matthews et al. 2014; Sutherland et al. 2016; Moulin et al. 2018; Hughes et al. 2020) and numerical modeling studies (Sarkar and Pham 2019; Large and Caron 2015) have provided a consistent picture of the physical processes determining the evolution of DWLs in the ocean: strong surface buoyancy forcing tends to suppress turbulence below the DWL and induce a near-surface trapping of momentum, reflected in the evolution of a near-surface diurnal jet with speeds $\mathcal{O}(0.1)$ m s^{-1}. The strong shear at the lower edge of the diurnal jet generates a marginally stable stratified shear layer, triggering strong DWL turbulence and entrainment (Hughes et al. 2020).

This detailed understanding of the DWL dynamics was, however, almost exclusively gained based on investigations and long-term studies at tropical latitudes (e.g., Matthews et al. 2014; Bellenger and Duvel 2009), despite the observation that during the summer months diurnal SST anomalies at high latitudes may be as large as those found in tropical regions (Kawai and Wada 2007). The few available studies of high-latitude DWLs (e.g., Eastwood et al. 2011; Jia et al. 2023) found a wide-spread occurrence also in the Arctic Ocean. Jia et al. (2023) reported a repeated occurrence of DWLs with significant warming amplitudes > 2°C, including extreme events with amplitudes > 5°C, during the two summer months of their measurement campaign at latitudes of up to 80°N. A recent evaluation of turbulence models, including their performance under strong diurnal warming (Johnson et al. 2023), was for a low-latitude DWL. Due to the lack of detailed observations and numerical studies of high-latitude DWLs, our understanding of the energetics and parameterization of these features is limited at the moment.

A few recent studies focusing on the impact of surface-wave effects on DWLs (Kukulka et al. 2013; Pham et al. 2023; Wang et al. 2023) underlined the importance of Langmuir Turbulence (LT) for the evolution of diurnal near-surface stratification, typically identifying a reduction of the diurnal SST amplitude and an increase of the DWL thickness due to stronger mixing. The ability of existing parameterizations (Price et al. 1986; Fairall et al. 1996) and ocean turbulence models to reproduce these effects has not been systematically evaluated so far.

The goal of this paper is to investigate the relevance, implications, and parameterizations of different processes (in particular: LT and rotation effects in high-latitude DWLs) across the entire physically relevant parameter space. Section 2 introduces the models used in this study. Most of the analysis is based on a second-moment turbulence model that includes the effects of LT. To validate this model and evaluate its performance concerning the effects of LT, we use Section 3 to compare it to our LES results for a typical DWL scenario. After that, in Section 4, we use our validated second-moment model to investigate DWL energy budgets in a typical tropical vs a high-latitude DWL, thereby focusing especially on the effects of rotation and day length that have so far received only little attention. Lastly, in Section 5, we attempt to provide a unified description of DWLs in the ocean by first identifying the key non-dimensional parameters that govern their structure and evolution, and then evaluating the influence of these parameters across a large parameter space. Here, we also test the applicability of the frequently used bulk parameter model by Price et al. (1986) for high-latitudes and DWLs influenced by LT.

2. Model formulation

a. Momentum and buoyancy equations

Our analysis will be based on the one-dimensional transport equations for momentum and buoyancy for an infinitely deep water column,

$$\frac{\partial u}{\partial t} - f(v + v_s) = \frac{\partial}{\partial z}\left(\nu \frac{\partial u}{\partial z}\right) - \frac{\partial \tau_x}{\partial z} \tag{1}$$

$$\frac{\partial v}{\partial t} + f(u + u_s) = \frac{\partial}{\partial z}\left(\nu \frac{\partial v}{\partial z}\right) - \frac{\partial \tau_y}{\partial z} \tag{2}$$

$$\frac{\partial b}{\partial t} = \frac{\partial}{\partial z}\left(\nu^b \frac{\partial b}{\partial z}\right) - \frac{\partial G}{\partial z} + \frac{\partial I_b}{\partial z}\,, \tag{3}$$

where u and v are the Reynolds-averaged velocities in the x- and y-directions, u_s and v_s the corresponding Stokes drift velocities, f the Coriolis parameter, and ν and ν^b the molecular diffusivities of momentum and buoyancy (or heat), respectively. The vertical turbulent momentum fluxes (normalized here with a constant reference density $\rho_0 = 1027$ kg m^{-3}) are denoted by τ_x and τ_y. The evolution of the Reynolds-averaged buoyancy, b, is determined by the vertical turbulent buoyancy flux, G, and the radiative buoyancy flux, I_b, due to penetrating short-wave radiation. We use the conventions that z points vertically upward with $z = 0$ at the surface, that all turbulent fluxes are positive upward, and that the radiative buoyancy flux I_b is positive downward.

As boundary conditions for the momentum equations in (1) and (2), we describe the components of the (normalized) wind stress, τ_x^0 and τ_y^0, at the surface. Similarly, for the buoyancy equation in (3), we prescribe the non-solar surface buoyancy flux $B_0 = \alpha g Q_{ns}/(\rho_0 c_p)$ at $z = 0$, where Q_{ns} (positive downward) is the non-solar heat flux, accounting for the long-wave, latent, and sensible heat fluxes. Here, g is the acceleration of gravity, c_p the specific heat capacity, and α the thermal expansion coefficient. Note that Q_{ns} and B_0 will generally be negative (surface heat loss) in our study. Zero-flux conditions for the turbulent fluxes of momentum and buoyancy are applied at $z \to -\infty$ (practically, the lower boundary conditions are imposed at some finite value of z that is sufficiently far below the surface to not affect the results).

b. Surface forcing

In order to identify the key parameters controlling the DWL evolution and structure, the following analysis will be based on idealized atmospheric fluxes that reflect the essential characteristics of the atmospheric forcing under conditions favorable for DWLs. This forcing consists of a constant non-solar heat (or buoyancy) loss at the surface ($B_0 < 0$), and a periodic diurnal variability induced by the radiative heat flux according to

$$I_0(t) = \max\left(0,\ I_{\max} \cos\left[\frac{\pi}{T_d}(t - \frac{T_p}{2})\right]\right) , \tag{4}$$

where T_p is the period of the prescribed forcing (24 hours), T_d the duration of the daylight period with $I_0 > 0$, and $I_{\max}$ the maximum radiative heat flux reached at $T_p/2$ (midday). We performed numerical tests in which we compared this simplified solar radiation model with a more realistic radiation expression based on Stull (1988) and found only small differences in the DWL evolution

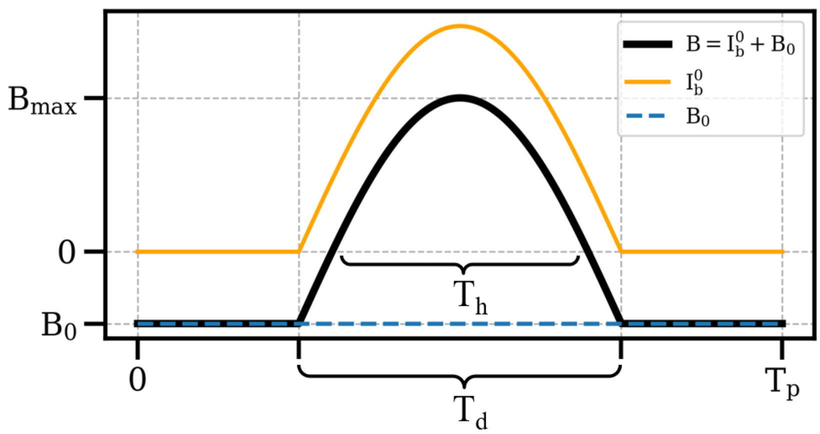

FIG. 1. Idealized buoyancy forcing with the radiative buoyancy flux at the surface, I_b^0, the non-solar surface buoyancy flux, B_0, and their sum, the total surface buoyancy flux B. Note that here we show the special case for which $T_d = T_p/2$.

that did not affect any of our conclusions. For our idealized study focusing on the basic mechanisms of DWL formation, the downward short-wave radiation I will be computed from a simple absorption model of the form

$$I(z) = I_0 e^{\frac{z}{\eta}} , \tag{5}$$

where η is the short-wave absorption scale. Note that in Section 3 (model validation), and in some parts of the parameter space study in Section 5, we will make the additional simplifying assumption that $\eta = 0$, i.e. that all radiation is absorbed at the surface. The radiative buoyancy flux I_b in (3) follows from

$$I_b = \frac{\alpha g}{\rho_0 c_p} I . \tag{6}$$

The temporal evolution of the surface buoyancy flux B_0, the radiative buoyancy flux at the surface $I_b(z=0) = I_b^0$, and their sum (the total surface buoyancy flux B), are shown in Fig. 1.

The surface buoyancy forcing defined this way is completely described by four dimensional parameters: the two time scales T_p and T_d, the maximum total surface buoyancy flux at midday, $B_{\max}$, and the surface buoyancy loss B_0. Rather than T_d, the more sensible parameter to describe the formation of DWLs is the heating period T_h during which the total surface buoyancy flux B is positive (see Fig. 1). From (4), it is clear that these two time scales are related according to

$$T_h = \frac{2T_d}{\pi} \arccos\left(\frac{B_0}{B_0 - B_{\max}}\right) . \tag{7}$$

All our simulations will be forced by a constant wind stress in the x-direction, $\tau_x^0 = C_d \frac{\rho_a}{\rho_0} U_{10}^2$, where $\rho_a = 1.23$ kg m^{-3} is the air density, U_{10} the 10-meter wind speed, and $C_d = 1.7 \cdot 10^{-3}$ a constant drag coefficient. Introducing the friction velocity, $u_* = \sqrt{|\tau_x^0|}$, as another key dimensional parameter of the problem, the quadratic drag law can also be expressed as $u_*^2 = C_d(\rho_a/\rho_0)U_{10}^2$.

Finally, surface wave parameters used to calculate the Stokes drift in our study are computed from the "Theory Wave" approach of Li et al. (2017). In brief, this model accounts for contributions to the Stokes drift profile from the entire frequency band of the theoretical wave spectrum of Phillips (1958), ignoring swell but including the effects of directional spreading. The surface Stokes drift velocity, u_s^0, and the Stokes transport, V_s, are estimated from expressions of the form

$$u_s^0 = c_s U_{10} \, , \quad V_s = C_s g U_{10}^3 \, , \tag{8}$$

where $c_s = 0.016$ and $C_s = 2.67 \cdot 10^{-5}$ s^4 m^{-2} are model constants. From these expressions, and the quadratic drag law mentioned above, the turbulent Langmuir number $\mathrm{La} = (u_*/u_s^0)^{\frac{1}{2}}$, defined by McWilliams et al. (1997), can also be expressed as $\mathrm{La} = (\rho_a C_d)^{\frac{1}{4}}/(\rho_0 c_s^2)^{\frac{1}{4}}$. Note that this yields a constant $\mathrm{La} = 0.3$, as typical for equilibrium wave fields.

As shown by Li et al. (2017), the profile of the Stokes velocity u_s predicted by their model is a function of the surface Stokes velocity, u_s^0, and the spectral peak wave number defined as

$$k_p = 0.176 \frac{u_s^0}{V_s} \, . \tag{9}$$

For the exact expressions of the Stokes velocity profile, $u_s(z, u_s^0, k_p)$, which we use to compute the Stokes shear in our model, please refer to Li et al. (2017) or Section 1 of the supplemental material.

c. Second-moment turbulence modeling approach

In our second-moment turbulence modeling approach, which is validated in Section 3 and then used for all of the analyses in Sections 4 and 5, the turbulent momentum fluxes appearing in (1) and (2) are computed from down-gradient expressions of the form

$$\tau_x = \langle u'w' \rangle = -\left(\nu_t \frac{\partial u}{\partial z} + \nu_t^S \frac{\partial u_s}{\partial z} \right) , \quad \tau_y = \langle v'w' \rangle = -\left(\nu_t \frac{\partial v}{\partial z} + \nu_t^S \frac{\partial v_s}{\partial z} \right) , \tag{10}$$

where primes and bracket denote turbulent fluctuations and ensemble averages, and ν_t and ν_t^S the vertical turbulent diffusivities of momentum related to the Eulerian and Stokes velocities, respectively (Harcourt 2013, 2015). Similarly, the vertical turbulent buoyancy flux in (3) is computed from

$$G = \langle w'b' \rangle = -\nu_t^b \frac{\partial b}{\partial z} = -\nu_t^b N^2 , \tag{11}$$

with the vertical turbulent diffusivity ν_t^b and the squared buoyancy frequency $N^2 = \partial b / \partial z$.

As discussed in more detail in Appendix A1, the turbulent diffusivities are assumed to be proportional to a turbulence length scale, l, and a turbulent velocity scale, $k^{1/2}$, where $k = \overline{u_i' u_i'}/2$ is the turbulence kinetic energy (TKE) computed from a transport equation of the form

$$\frac{\partial k}{\partial t} = D_k + P + P_s + G - \varepsilon , \tag{12}$$

generalized here to also account for the effects of LT. Here, D_k denotes the vertical transport of TKE and ε the turbulence dissipation rate. P and P_s are the Eulerian and Stokes shear production terms defined as (Harcourt 2013, 2015):

$$P = -\langle u'w' \rangle \frac{\partial u}{\partial z} - \langle v'w' \rangle \frac{\partial v}{\partial z} = \nu_t S^2 + \nu_t^S S_c^2 , \tag{13}$$

$$P_s = -\langle u'w' \rangle \frac{\partial u_s}{\partial z} - \langle v'w' \rangle \frac{\partial v_s}{\partial z} = \nu_t S_c^2 + \nu_t^S S_s^2 , \tag{14}$$

where

$$S^2 = \left(\frac{\partial u}{\partial z} \right)^2 + \left(\frac{\partial v}{\partial z} \right)^2 , \quad S_c^2 = \frac{\partial u}{\partial z} \frac{\partial u_s}{\partial z} + \frac{\partial v}{\partial z} \frac{\partial v_s}{\partial z} , \quad S_s^2 = \left(\frac{\partial u_s}{\partial z} \right)^2 + \left(\frac{\partial v_s}{\partial z} \right)^2 . \tag{15}$$

Finally, the turbulent length scale l, required for the computation of the turbulent diffusivities, is inferred from the solution of a Mellor-Yamada-type transport equation for the product kl in (A2) or, alternatively for comparison, from a transport equation for the inverse turbulence time scale

$\omega \propto k^{1/2} l^{-1}$ in (A4). All relevant details of the turbulence closure models used in our study are summarized in A1.

d. LES modeling approach

The LES approach is used to validate the second-moment models in Section 3. The approach is based on the Craik-Leibovich equations to produce the Eulerian velocity,pressure and buoyancy fields in a temporally-evolving three-dimensional computational domain. Readers are referred to Appendix A2 for the numerical implementation of the LES and the model setup.

From the LES, horizontally-averaged profiles of velocities, $\langle U_i \rangle$, buoyancy, $\langle B \rangle$, and turbulent fluxes, $\left\langle U_i' U_j' \right\rangle$, are obtained and used to compare with the second-moment turbulence model outputs (e.g., u, v, and b) in (1)-(3), as elaborated in Section 3. Here, we use angle brackets to denote the horizontal average of the LES fields and primes to denote the fluctuations.

3. Comparison of LES and second-moment models

In this section, we compare the second-moment turbulence closure models to our LES results for a typical tropical DWL scenario both with and without the effects of LT, focusing especially on the performance of the second-moment model for this newly included process. Both LES and second-moment models are driven with identical atmospheric and buoyancy forcing and use the same parametric surface-wave model by Li et al. (2017) to compute the Stokes velocities. Note that the effects of surface-wave breaking are not taken into account in our simulations.

The three different second-moment models that we want to test are described in detail in Section 2c and Appendix A1. They include: (a) the full model of Harcourt (2015, hereafter H15), which represents LT effects in both the stability functions and the transport equations for k and kl in equations (12) and (A2) through the additional Stokes production term P_s; (b) the model of Kantha and Clayson (2004, hereafter KC04), which only considers the additional Stokes production terms in the transport equations but ignores the impact of LT on the stability functions; and (c) the model of Kantha and Clayson (1994), which ignores LT effects entirely. Both the models of H15 and KC04 converge to the model of Kantha and Clayson (1994) for the special case of zero Stokes drift ($u_s = 0$), which allows for a clear separation of LT effects from other modeling components. To compute the turbulent length scale l, we used an extended version of the Mellor-Yamada equation for kl in (A2) for all of the following simulations but we will also include a short comparison with a modified version of the k-ω model in Section 2 of the supplemental material.

All second-order moment model simulations were conducted with a modified version of the General Ocean Turbulence Model (GOTM), described in Umlauf et al. (2005). The time step for these simulations was set to 6 s, and the domain depth and grid size match those of the LES grid with a resolution of 0.05 m at the surface, gradually coarsening towards the bottom (see Appendix A2). These parameters were found to ensure numerical convergence and exclude any impact of the lower edge of the domain on the DWL properties.

For all the simulations in this section, we use a peak solar buoyancy flux of $I_b = 2.3 \cdot 10^{-7}$ m^2 s^{-3} at noon at the surface (see Fig. 1), which, for comparison, would correspond to a peak solar heat flux of $I_{\mathrm{max}} = 400$ W m^{-2} for a thermal expansion coefficient $\alpha = 2.4 \cdot 10^{-4}$ K^{-1}. To keep the setup for this model comparison as simple as possible, we also assume that the non-solar surface buoyancy flux vanishes ($B_0 = 0$) and that all short wave radiation is absorbed at the surface ($\eta = 0$). The heating period is $T_h = T_d = 12$ h at a tropical latitude of 10°N (corresponding to $f = 2.53 \cdot 10^{-5}$ s^{-1} and a local inertial period of $T_f = 69.1$ h). A constant friction velocity of $u_* = 4.4 \cdot 10^{-3}$ m s^{-1} is applied, equivalent to a wind speed of $U_{10} = 3.1$ m s^{-1}. This results in a Monin-Obukhov length $L_{\mathrm{MO}} = u_*^3/(\kappa B) = 0.93$ m at midday (with $\kappa = 0.4$), which is more than an order of magnitude larger than the numerical grid spacing near the surface. For all GOTM runs in this section, the surface roughness length z_0 that appears in the boundary condition (A9) for the turbulence length scale l was set to $z_0 = 0.01$ m. This model parameter is not well constrained. Our parameter studies in Section 5 show, however, that the impact of z_0 is negligible.

To save computational resources for the LES, all simulations in this section start at 05:00 in the morning (one hour before the start of the radiative buoyancy forcing) rather than at midnight. Note, however, that in all the following sections, the beginning of the simulations is at midnight.

The horizontally averaged LES results are shown in Fig. 2, comparing simulations without ($u_s = 0$) and with LT. In both cases, the buoyancy structure (Fig. 2a,b) shows the evolution of DWLs with similar characteristics. LT effects are clearly noticeable especially in the reduced near-surface buoyancy in the simulation with wave forcing, which is consistent with the reduced near-surface stratification due to LT-enhanced mixing (Fig. 2c,d). The Eulerian shear (Fig. 2e,f) in the simulation with LT deviates from its counterpart with $u_s = 0$ significantly in the upper 2 m,

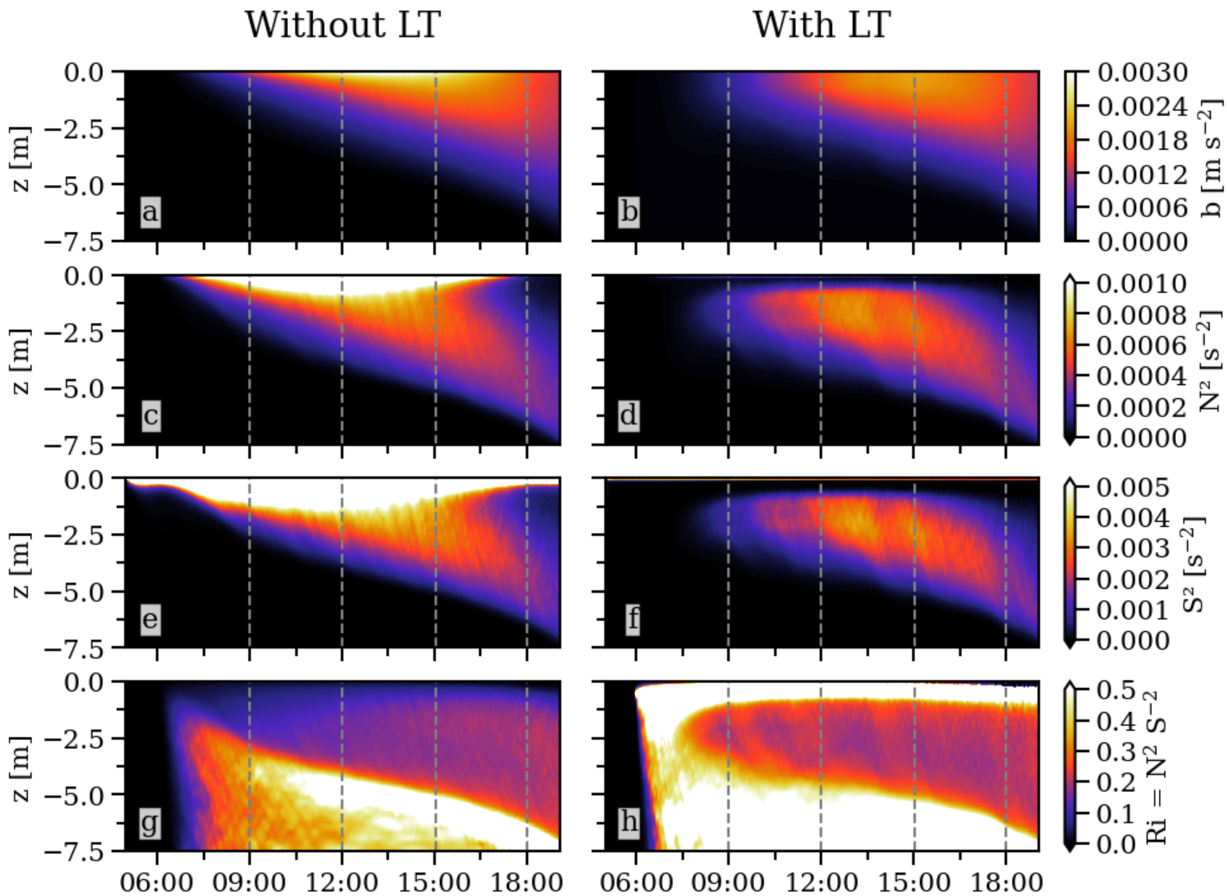

Fig. 2. Evolution of (a,b) buoyancy, (c,d) buoyancy frequency squared, (e,f) total Eulerian shear squared, and (g,h) gradient Richardson number for a typical DWL scenario without (left) and with LT forcing, respectively. Shown are horizontally averaged LES results for the forcing parameters discussed in Section 3. Dashed vertical lines mark the profiles shown in Figs. 3 and 4.

where the Stokes shear production P_s becomes the dominant source of turbulence (u_s decays to approximately 10% of its surface value within the uppermost 0.65 m). This effect is also clearly evident in the Richardson number, $Ri = N^2 S^{-2}$, which does not account for Stokes shear (Fig. 2g,h).

Figs. 3 and 4 compare the DWL evolution in the LES (with and without LT) and the second-moment models for four selected points in time (marked in Fig. 2). This comparison shows that the overall characteristics of the LES are well reproduced by all models: both the DWL thicknesses and the vertical structures of buoyancy, velocity, and the turbulent momentum flux closely correspond to those predicted by the LES. Significant differences are largely confined to the upper 1-2 m,

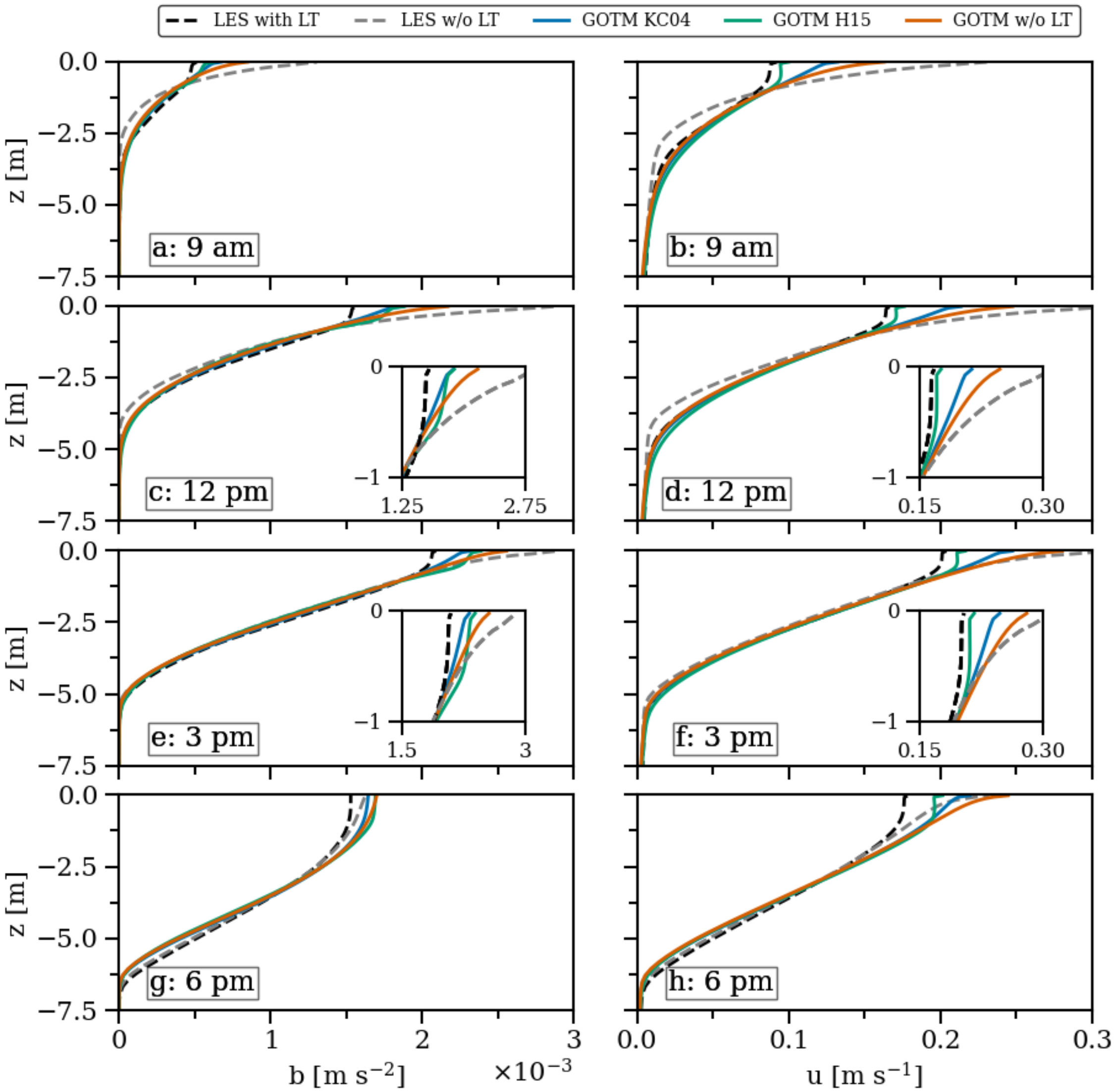

FIG. 3. Comparison of LES and GOTM simulations for (a,c,e,g) buoyancy and (b,d,f,h) u-component of the velocity at the times indicated in Fig. 2. Dashed lines show LES results with (black) and without (gray) LT. Colored lines correspond to different second-moment models as indicated in the legend. Inlays panels in (c-f) show enlarged views of the near-surface region.

where the LES suggest a strong reduction of stratification and shear due to the effects of LT. For the period between 12:00 and 15:00, when DWL anomalies are most distinct, the inlay plots in Fig. 3d,f show that the inclusion of LT effects leads to a significant reduction of the near-surface velocity. Only the model of H15 is in close agreement with the LES, while the model of KC04 clearly

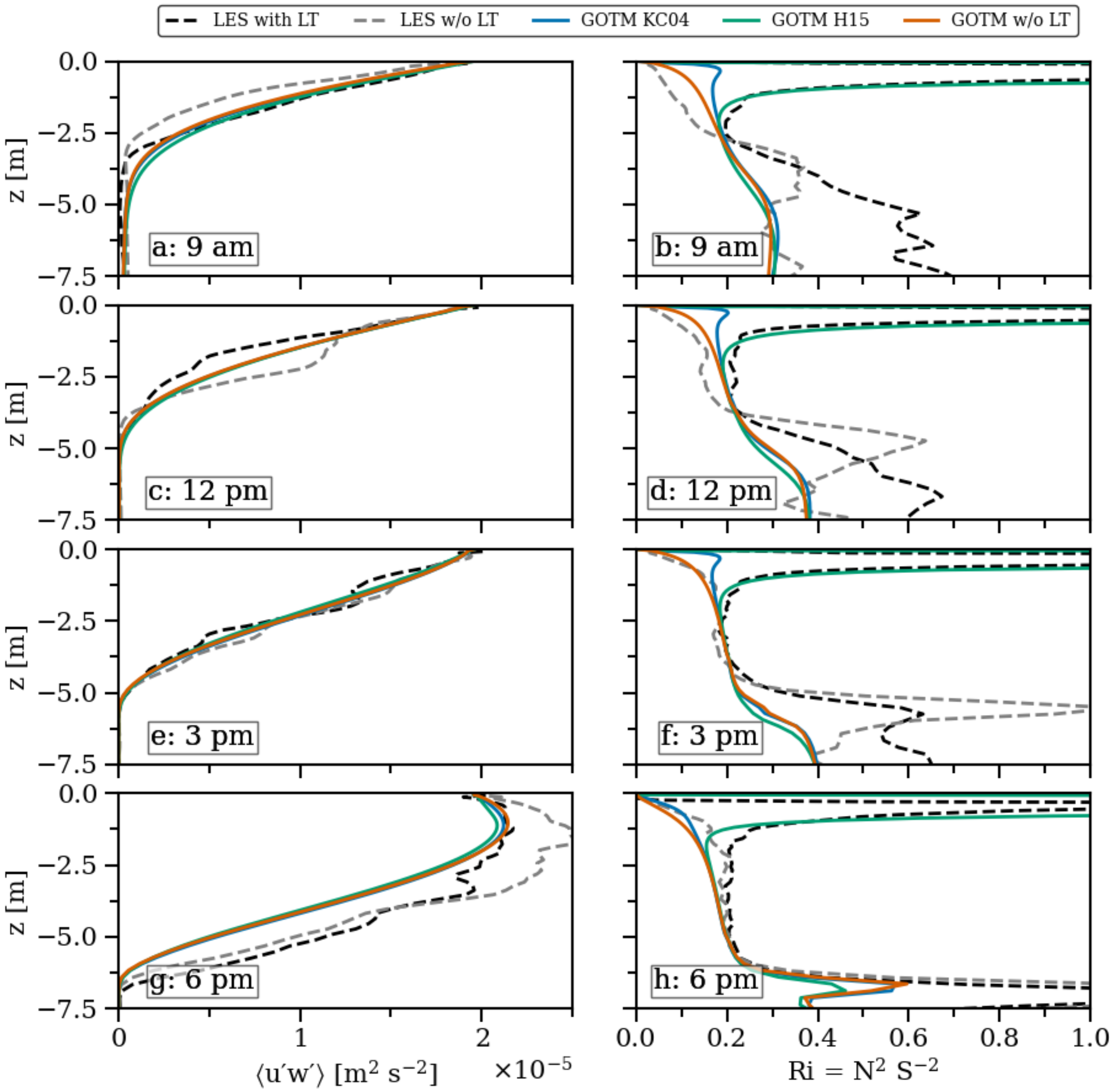

FIG. 4. As in Fig. 3 but now for (a,c,e,g) total (resolved plus subgrid-scale) turbulent momentum flux $\langle u'w' \rangle$ and (b,d,f,h) gradient Richardson number Ri.

underestimates the additional mixing of momentum due to LT effects, underlining the importance of the Stokes shear term in (10). For the near-surface buoyancy profiles (see inlay plots in Fig. 3c,e), differences between the second-moment models are less pronounced, and all tend to underestimate the reduction of near-surface stratification due to LT. Differences between the simulations with and without LT become especially clear in the gradient Richardson number shown in Fig. 4b,d,f,h. The pronounced near-surface peak in Ri is captured only by the most advanced model of H15 as shown in Fig. 4.

It is worth noting that all second-moment models predict virtually identical profiles underneath the thin near-surface region directly affected by Stokes production. For the LES, the negligible effect of LT below the thin-surface layer is the case only for the late-stage DWLs (Fig. 3e-g), while the DWL evolution in the morning and around noon (Fig. 3a-d) shows weak but significant LT effects also below the Stokes layer. These LT effects on the mean fields are accompanied by inflectional shear, similar to observations of inflectional shear by Hughes et al. (2021) when convective cooling commenced at sundown, as well as by enhanced TKE transport from the Stokes layer towards the layer underneath (Li and Fox-Kemper 2020).

Overall, we conclude that the performance of the model of H15 is most satisfying, and we will therefore use this model for all of the following numerical investigations. As shown in Section 2 of the supplemental material, simulations conducted with a modified version of the k-ω model (see Appendix A1), using the same stability functions of H15, yield very similar results, providing support for the robustness of our results.

4. DWL energy budgets at low and high latitudes

In this section, we derive energy budgets for DWLs and use these to investigate the effects of rotation and heating time on high latitude DWLs.

a. Theory

For the analysis of the DWL energetics, it is convenient to define a DWL-averaged buoyancy, $\overline{b}$, and a DWL thickness, h, based on expressions of the form

$$\overline{b} h = \int_{z_\mathrm{ref}}^{0} \tilde{b} \mathrm{d}z \tag{16}$$

and

$$\varphi \overline{b} h^2 = -\int_{z_\mathrm{ref}}^{0} \tilde{b} z \mathrm{d}z \, , \tag{17}$$

where $\tilde{b} = b - b_{\text{ref}}$ is the DWL buoyancy anomaly, referenced with respect to the buoyancy b_{ref} at some reference level z_{ref} below the DWL, and φ a shape factor that depends on the vertical structure of the buoyancy profile. E.g., it can be shown that $\varphi = 1/2$ and $\varphi = 1/3$ correspond to the cases of well-mixed and linearly stratified DWLs, respectively. For comparison, it is worth noting that Fairall et al. (1996) assumed DWLs with linear stratification ($\varphi = 1/3$), whereas applying (16) and (17) to the empirical DWL profiles in expression (17) of Gentemann et al. (2009) yields $\varphi \approx 0.2 - 0.4$ with a transition from exponential to more well-mixed profiles depending on wind speed. In our model, φ changes in time during the evolution of the DWL.

Reformulating (3) in terms of $\tilde{b}$, ignoring the molecular fluxes, and integrating the resulting equation vertically between z_{ref} and the surface, the time derivative of the relation in (16) can be expressed as

$$\frac{\mathrm{d}(\overline{b}h)}{\mathrm{d}t} = \frac{\mathrm{d}}{\mathrm{d}t}\int_{z_{\text{ref}}}^{0} \tilde{b}\,\mathrm{d}z = B_0 + I_b^0 \,, \tag{18}$$

which reflects the heat budget of the DWL, expressed in terms of buoyancy. In the derivation of (18), we have assumed that the temporal variability of the reference buoyancy, b_{ref}, has a negligible effect. Our idealized simulations show that the variability of b_{ref} indeed becomes negligible shortly after the DWL has formed, isolating the reference level from surface buoyancy forcing.

The expression in (17) is recognized as the potential energy anomaly, E_{pot}, induced by the presence of the DWL. Reformulating (3) in terms of $\tilde{b}$, multiplying the result by z, and integrating by parts, yields an equation for the evolution of the potential energy anomaly:

$$\frac{\mathrm{d}}{\mathrm{d}t}E_{\text{pot}} = \frac{\mathrm{d}(\varphi\overline{b}h^2)}{\mathrm{d}t} = -\frac{\mathrm{d}}{\mathrm{d}t}\int_{z_{\text{ref}}}^{0} \tilde{b}z\,\mathrm{d}z = -\int_{z_{\text{ref}}}^{0} G\,\mathrm{d}z + h\overline{I}_b \,, \tag{19}$$

where we again ignored the molecular fluxes and introduced $\overline{I}_b = h^{-1}\int_{z_{\text{ref}}}^{0} I_b\mathrm{d}z$. In the derivation of (19), we have assumed $I_b(z_{\text{ref}}) \ll I_b^0$ to ensure that our analysis includes the entire near-surface region with significant radiative heating. Similar to (18), the effect of the temporal variability of b_{ref} is found to be negligible in our simulations and has therefore been neglected in (19).

Using (18), the energy budget in (19) can thus be re-arranged in the form

$$\underbrace{\varphi h(B_0+I_b^0-\frac{\overline{I}_b}{\varphi})}_{\substack{\text{work required to}\\ \text{mix down buoyancy}\\ \text{added near surface}}} + \underbrace{\varphi h\overline{b}w_e}_{\substack{\text{work required}\\ \text{to mix up}\\ \text{entrained fluid}}} + \underbrace{\frac{\mathrm{d}\varphi}{\mathrm{d}t}\overline{b}h^2}_{\substack{\text{work required to}\\ \text{change the DWL}\\ \text{buoyancy structure}}} = \underbrace{-\int_{z_\mathrm{ref}}^{0} G\mathrm{d}z}_{\substack{\text{work done}\\ \text{by turbulence}}} , \tag{20}$$

where we introduced the entrainment velocity $w_e = \mathrm{d}h/\mathrm{d}t$.

Similarly, an equation for the DWL kinetic energy can be obtained by multiplying the momentum equations in (1) and (2) with u and v, respectively, adding the results, and integrating from z_ref to the surface. Ignoring again the molecular flux terms for simplicity, this yields an energy budget of the form:

$$\frac{\mathrm{d}}{\mathrm{d}t}E_k = \frac{\mathrm{d}}{\mathrm{d}t}\int_{z_\mathrm{ref}}^{0} \frac{u^2+v^2}{2}\mathrm{d}z = \mathbf{u}^0\cdot\boldsymbol{\tau}^0 + \int_{z_\mathrm{ref}}^{0} f\mathbf{k}\cdot(\mathbf{u}\times\mathbf{u}_s)\,\mathrm{d}z - \int_{z_\mathrm{ref}}^{0} P\mathrm{d}z , \tag{21}$$

where $\mathbf{k}$ is the upward unit vector and $\mathbf{u}^0$ the velocity at the surface. The terms on the right hand side of (21) can be interpreted as: (a) the work performed by the wind stress on the DWL, (b) the exchange of kinetic energy with the surface wave field due to the effect of rotation (see, e.g., Suzuki and Fox-Kemper 2016), and (c) the loss of kinetic energy to TKE by turbulence shear production. Similar to the negligible effect of temporal variations of b_ref in (18) and (19), we also find that the temporal variability of the reference kinetic energy, $(u_\mathrm{ref}^2+v_\mathrm{ref}^2)/2$, has a negligible effect on the energy budget in (21) shortly after the DWL has formed. Therefore this term has been omitted in (21).

The shear production term in (21) connects the DWL kinetic energy to the vertically integrated TKE equation,

$$-\int_{z_\mathrm{ref}}^{0} G\mathrm{d}z = -\frac{\mathrm{d}}{\mathrm{d}t}\int_{z_\mathrm{ref}}^{0} k\mathrm{d}z + \int_{z_\mathrm{ref}}^{0} (P+P_s)\mathrm{d}z - \int_{z_\mathrm{ref}}^{0} \varepsilon\mathrm{d}z , \tag{22}$$

which is easily derived from (12). The left hand side of (22) and the right hand side of the potential energy budget in (20) are identical, showing that the energy available for mixing within the DWL corresponds to the fraction of the (mean flow and Stokes) shear production that is neither dissipated nor used to change the DWL integrated TKE. The relative importance of the various terms in the DWL energy budgets in (20), (21), and (22) will be investigated in the following discussion.

TABLE 1. Atmospheric forcing and model parameters used for the analysis of the DWL energetics.

	$B_{\max}$ [m^2 s^{-3}]	B_0 [m^2 s^{-3}]	U_{10} [m s^{-1}]	L_{MO} [m]	T_f [h]	T_h [h]	z_0 [m]	η [m]	k_p [m^{-1}]
10°N	$5.5 \cdot 10^{-7}$	$-2.6 \cdot 10^{-7}$	3.1	0.39	69.1	9.5	0.01	0.87	1.13
70°N	$1.4 \cdot 10^{-7}$	$-1.2 \cdot 10^{-7}$	3.1	1.53	12.6	12.2	0.01	0.87	1.13

b. Results

To investigate the DWL energy budgets derived above, we compare a typical tropical case at 10°N with a high-latitude DWL at 70°N. The results were obtained using GOTM with the turbulence closure model of H15 that was shown to compare favorably to the LES in the previous section. We used a time step of 6 s and a grid spacing of 0.015 m at the surface, gradually coarsening towards the lower end of the numerical domain at 50 m depth. The atmospheric forcing and model parameters are summarized in Tab. 1. For both cases, we assumed that the surface buoyancy loss B_0 due to cooling exactly compensates the radiative buoyancy supply over the course of a day. The buoyancy forcing parameters in Tab. 1 were chosen to yield realistic summertime values for the peak radiative heat flux $I_{\max}$ for the corresponding latitudes, water temperatures and thermal expansion coefficients. For the tropical case, the values in Tab. 1 correspond to $I_{\max} = 1000$ W m^{-2}, using $\alpha = 3.4 \cdot 10^{-4}$ K^{-1} for tropical 30°C water temperatures. Analogously, the parameters for the high-latitude case yield $I_{\max} = 680$ W m^{-2} with $\alpha = 1.6 \cdot 10^{-4}$ K^{-1} for 10°C water temperatures. Since the buoyancy flux is linearly proportional to α, it can correspond to different heat fluxes, depending on water temperature. To make our model more generally applicable, we have therefore formulated it in terms of buoyancy rather than temperature.

For the tropical case, as before, the period with non-zero solar radiation was chosen as $T_d = 12$ h (between 6:00 h and 18:00 h), whereas we assume $T_d = 18$ h (between 3:00 h and 21:00 h) for the high-latitude case. The resulting effective heating periods T_h, computed from (7), can be found in Tab. 1, together with all other model parameters that were kept constant. To determine the shortwave absorption length η in (5), we varied η and compared our GOTM results for the tropical scenario against a plot of the parametric temperature profile from equation (17) of Gentemann et al. (2009), who used a more complex nine-band absorption model for clear tropical waters. We find that our simple one-band model results in a very similar vertical DWL structure for $\eta = 0.87$ m, which is the value we used for all simulations in this section (Tab. 1).

The evolution of the near-surface buoyancy for the two cases is shown in Figs. 5a and 6a. The DWL thickness, h, one of the most important bulk parameters, is defined here by a simple density threshold, identifying the lower edge of the DWL with the vertical position where the buoyancy has decayed to 5% of its maximum value. Figs. 5a and 6a show that this definition provides a plausible representation of the vertical extent of the DWL for both cases.

The reference level z_{ref} is chosen to coincide with the location of the minimum buoyancy in the water column, and $\tilde{b} = b - b_{\text{ref}}$ is defined based on the reference buoyancy b_{ref} found at this depth. This definition guarantees that the entire near-surface region affected by radiative heating is included in our analysis.

Fig. 5b shows the evolution of the kinetic energy budget in (21) for the tropical case. During the initial DWL formation phase until approximately early afternoon, the work performed by the wind, $u^0 \cdot \tau_x^0$, is largely used to accelerate the DWL (compare to $\frac{\mathrm{d}}{\mathrm{d}t} E_k$) with a significantly smaller contribution used for turbulence shear production $\int P \mathrm{d}z$. In the afternoon, entrainment starts to become increasingly important (Fig. 5a), and additional energy is thus required to accelerate entrained fluid. As a consequence, the DWL kinetic energy increases at a slower rate while shear production becomes the dominant energy sink. After the surface buoyancy forcing collapses in the late afternoon and evening, the entrainment rate further increases as no more work is required to mix down buoyant fluid from the surface (see more detailed discussion below). This point is marked by a sharp transition in the energy budget at approximately 18:00, after which $\frac{\mathrm{d}}{\mathrm{d}t} E_k$ becomes insignificant, and the wind work is largely used for turbulence shear production that in turn becomes available for entrainment. Stokes shear production (Fig. 5c) dominates turbulence production during the initial DWL formation phase until approximately noon, while the exchange of mean kinetic energy with the wave field (marked in green in Fig. 5b) is negligible throughout the simulations.

For the high-latitude case shown in Fig. 6, the work performed by the surface stress, $u^0 \cdot \tau_x^0$, starts to be suppressed by the veering of the near-surface velocity out of the wind direction shortly after the formation of the DWL. This is reflected in a late-morning peak of the wind energy input, and a subsequent monotonic decay down to negative values (energy loss) around 14:00 in the afternoon (Fig. 6b). Therefore, starting from the early afternoon, the pool of DWL kinetic energy built up during the initial DWL formation in the morning becomes an increasingly important energy source

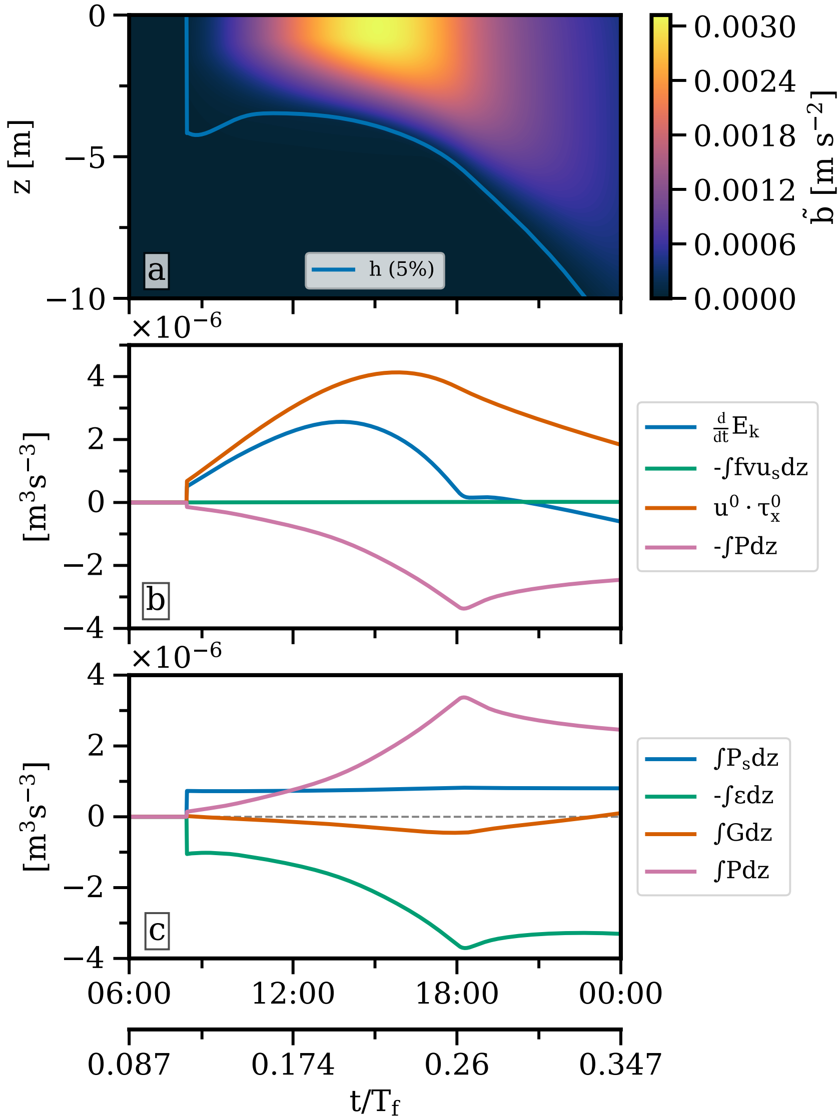

FIG. 5. Evolution of (a) DWL buoyancy anomaly, (b) DWL kinetic energy budget in (21), and (c) turbulent kinetic energy budget in (22) for the tropical case at 10°N (Tab. 1). The blue line in (a) shows the DWL thickness h computed from the depth at which the buoyancy has dropped to 5% of its maximum value. Note that the simulation starts at midnight ($t/T_f = 0$), and that both the wind stress and Stokes drift point into the x-direction ($\tau_y^0 = 0$ and $v_s = 0$).

$(\frac{\mathrm{d}}{\mathrm{d}t} E_k < 0)$ to feed turbulence shear production in the afternoon. Comparison with Fig. 5 shows that due to these effects, the integrated wind work is approximately a factor of five smaller compared

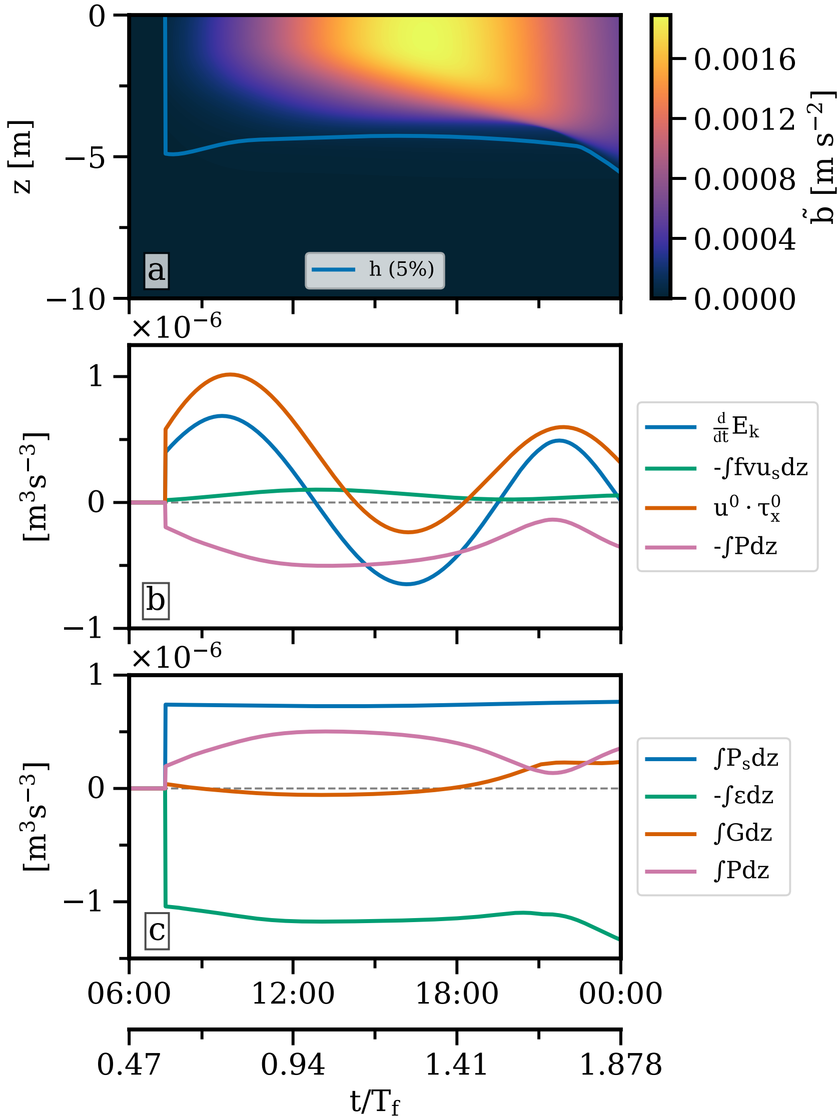

FIG. 6. As in Fig. 5 but now for the high latitude case at 70°N (Tab. 1). Note the different scales with respect to Fig. 5.

to the tropical case. Due to the overall strongly reduced energy turnover, the extraction of energy from the wave field due to Coriolis effects (green line in Fig. 6b) becomes significant in the mean kinetic energy budget, and Stokes shear production P_s exceeds Eulerian shear production P in the TKE budget. The net effect of the reduced turbulence production due to rotation is a complete collapse of entrainment after the initial DWL shoaling in the morning (blue curve in Fig. 6a).

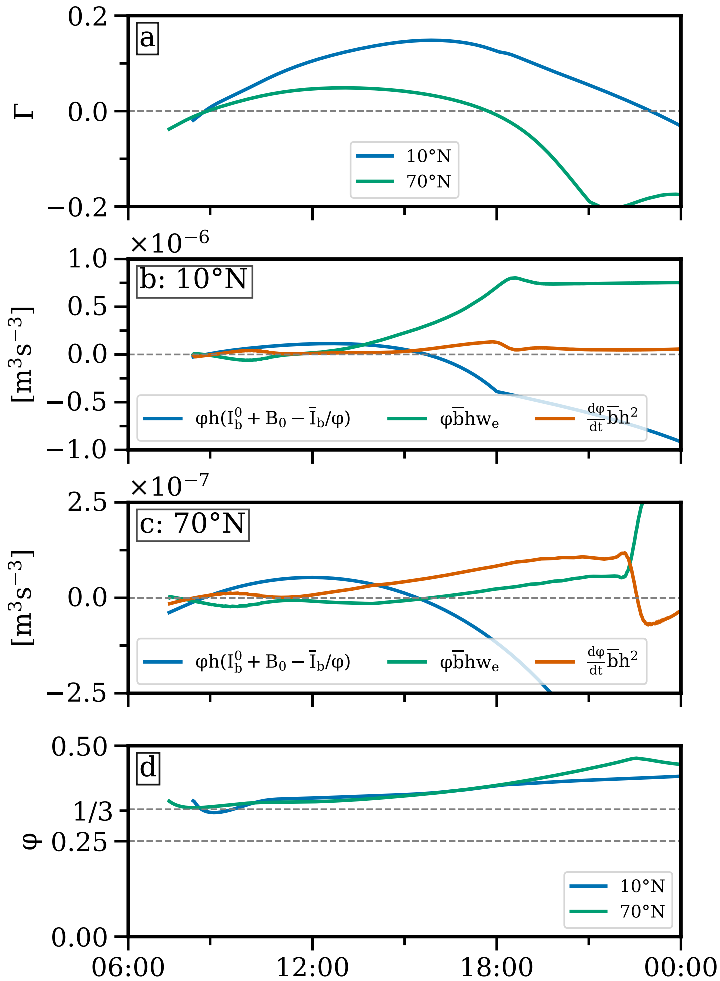

Fig. 7. Evolution of (a) bulk mixing efficiency Γ, the left hand side terms in (20) at (b) 10°N and (c) 70°N, (d) shape factor φ computed from (16) based on h from the 5% density threshold with the values of Fairall et al. (1996) and Gentemann et al. (2009) as dashed grey lines. Note the different axes scales in panels (b) and (c).

To investigate the extent to which the strong surface buoyancy forcing and the stratification inside the DWL affect the energetics of turbulence, we computed the bulk flux coefficient, $\Gamma = -\int_{z_{\mathrm{ref}}}^{0} G\mathrm{d}z / \int_{z_{\mathrm{ref}}}^{0} \varepsilon\mathrm{d}z$, and find strong differences between tropical and high latitudes. As shown in Fig. 7a, for the tropical case we find $\Gamma \approx 0.15$ during the late afternoon and evening, close to the popularly used value of $\Gamma = 0.2$. At high latitudes, however, Γ only reaches positive values during the time of strongest buoyancy forcing and the values are small compared to the tropical case. At later times, convection near the surface dominates the integral of the buoyancy production, causing it to change signs.

The different contributions to the potential energy budget in (20) for the tropical and high-latitude cases are compared in Fig. 7b and Fig. 7c, respectively. During midday, in both cases, the largest fraction of the work performed by turbulence against gravity is used to mix down near-surface buoyant fluid generated by solar heating. According to (20), the ratio $\overline{I}_b/(I_b^0\varphi)$ determines to what extent the work required for this process is reduced by the penetration of short-wave radiation. If all short-wave radiation is absorbed at the surface ($\eta = 0$), this ratio is zero. We find $\overline{I}_b/(I_b^0\varphi) = 0.53$ and $\overline{I}_b/(I_b^0\varphi) = 0.44$ at midday for the tropical and high-latitude cases, respectively, suggesting that penetrating short-wave radiation strongly impacts the DWL potential energy budget.

Fig. 7b and Fig. 7c also show that the first hours after the initial generation of the DWLs are characterized by "detrainment" ($w_e < 0$) due to the restratifying effect of the increasing solar radiation. For the tropical case, w_e changes sign in the late morning, and around 14:00 the work required for the entrainment of dense fluid at the DWL base finally becomes the dominating term in the potential energy budget. This is in strong contrast to the high-latitude case, in which entrainment never becomes an energetically relevant factor.

Beyond the work required for DWL deepening, turbulent mixing may also act to change the vertical DWL buoyancy structure. The energetic implications of this third type of energy conversion in (20) can be quantified by considering changes in the shape parameter φ, which is easily computed from (16) and (17) after determining the DWL thickness h from the 5% buoyancy threshold discussed above (see blue lines in Figs. 5a and 6a). Fig. 7d shows that during the morning and early afternoon, this parameter starts close to $\varphi = 1/3$, but increases to larger values over the course of the day, reflecting the tendency towards a more well-mixed DWL especially in the evening due to the decreasing solar buoyancy forcing. For comparison, the parametric temperature profiles in Gentemann et al. (2009) for this wind speed yield a constant $\varphi \approx 0.25$, whereas the model of Fairall et al. (1996) corresponds to a constant $\varphi = 1/3$. These differences in φ between our model and the models of Fairall et al. (1996) and Gentemann et al. (2009) can be largely attributed to the thin near-surface convective layer generated by penetrating short-wave radiation in our simulations, which is not represented in the models of Fairall et al. (1996) and Gentemann et al. (2009). Figs. 7b,c show that the work required for this partial homogenization of late-stage DWLs becomes significant only for the high-latitude case, where it dominates the potential energy balance during the afternoon.

5. Key parameters and DWL parameterization

a. Identification of dimensional and non-dimensional parameters

The evolution and physical properties of the DWLs in our idealized simulations are affected by a number of independent dimensional parameters, imposed by the atmospheric forcing and the properties of the surface wave field. The former includes the constant wind stress, quantified here with the help of the friction velocity u_* (or, equivalently, the wind speed U_{10}), and the parameters describing the idealized buoyancy forcing shown in Fig. 1: the maximum total buoyancy flux at midday, $B_{\max}$, the (constant) buoyancy loss at the surface B_0, the heating period T_h, and the period of the periodic forcing T_p. For penetrating short-wave radiation, the vertical absorption scale η in (5) has to be considered as an additional parameter.

The surface wave field affects the problem through the surface Stokes velocity, u_s^0, and a vertical decay scale that is determined by the peak wave number k_p. Note that the same two dimensional parameters would also appear for the more simple case of monochromatic waves (Kukulka et al. 2013). However, in the equilibrium wave model of Li et al. (2017) used in our study, both u_s^0 and k_p depend on the wind speed through (8) and (9), and therefore do not constitute independent dimensional parameters.

Finally, as all model parameters of the turbulence model are non-dimensional, no additional dimensional parameters are introduced - with a single exception: the upper boundary condition for the turbulent length scale l in (A9) involves the surface roughness length z_0 that we consider in the following as an additional independent parameter.

The most relevant velocity scale in our problem is the friction velocity u_*, which can be used to define the relevant length scale, $L = u_*^3/B_{\max}$ (note that this length scale is directly proportional to the Monin-Obhukov scale, $L_{MO} = u_*^3/(\kappa B)$, evaluated at midday). If we chose, in addition to u_* and L, the heating period T_h shown in Fig. 1 as the relevant time scale, we can non-dimensionalize the key variables of our problem (Tab. 2), and derive non-dimensional versions of the transport equations of momentum and buoyancy in (1)-(3). From these non-dimensional transport equations, it is straightforward to identify two key non-dimensional parameters of the problem. The first is the

Table 2. Definition of non-dimensional variables denoted by the ˆ symbol.

$z = \frac{u_*^3}{B_{\max}} \hat{z}$	$t = T_h \hat{t}$	$u, v = u_* \hat{u}, u_* \hat{v}$	$u_s, v_s = u_* \hat{u}_s, u_* \hat{v}_s$	$b = \frac{B_{\max}}{u_*} \hat{b}$	$k = u_*^2 \hat{k}$
$l = \frac{u_*^3}{B_{\max}} \hat{l}$	$\varepsilon = B_{\max} \hat{\varepsilon}$	$\nu_t = \frac{u_*^4}{B_{\max}} \hat{\nu}_t$	$\nu_t^b = \frac{u_*^4}{B_{\max}} \hat{\nu}_t^b$	$I_b = B_{\max} \hat{I}_b$	$f = \frac{\hat{f}}{T_h}$

non-dimensional Coriolis parameter, $\hat{f} = f T_h = 2\pi T_h / T_f$, which measures the ratio of the heating period and the inertial period, T_f. The second parameter,

$$R = \frac{u_*^2}{T_h B_{\max}} , \tag{23}$$

compares the destabilizing effect of the wind stress, u_*^2, to the stabilizing effect of the total buoyancy supply during the heating period (which is proportional to $T_h B_{\max}$). For simplicity, we ignore the molecular transport terms in (1)-(3) for our dimensional analysis, as their effect is only marginal in our simulations.

Additionally, the buoyancy flux ratio, $B_0/B_{\max}$, and the timescale ratio, T_h/T_p, appear as independent non-dimensional parameters in our model for the buoyancy forcing in Fig. 1. To reduce the number of free parameters and allow for quasi-periodic solutions, we will assume in most of the parameter studies that the daily average of the total buoyancy flux is zero, i.e. that the incoming solar radiation is exactly compensated by the net surface buoyancy loss $B_0 T_p$. With this constraint, B_0 and $B_{\max}$ are no longer independent:

$$-\frac{B_{\max}}{B_0} = \frac{\pi}{2} \frac{T_p}{T_d} - 1 , \tag{24}$$

and combining (7) and (24) thus yields

$$\frac{T_h}{T_p} = \frac{2}{\pi} \frac{T_d}{T_p} \arccos\left(\frac{2}{\pi} \frac{T_d}{T_p} \right) , \tag{25}$$

revealing a direct one-to-one relation between the timescale ratios T_h/T_p and T_d/T_p. The final non-dimensional parameter associated with the buoyancy forcing is the non-dimensional absorption scale, $\hat{\eta} = \eta / L$.

Finally, as pointed out in the context of (8) above, the wave model of Li et al. (2017) predicts a constant value of the Langmuir number $\mathrm{La} = (u_* / u_s^0)^{\frac{1}{2}} = 0.3$. The second non-dimensional product

TABLE 3. The non-dimensional parameters. Note that the variability of some parameters appearing in brackets is restricted on our model.

$R = \frac{u_*^2}{T_h B_{\max}}$	$\hat{f} = f T_h$	$\frac{T_h}{T_p}$	$\frac{B_0}{B_{\max}}$
$\hat{z}_0 = \frac{z_0}{L}$	$\hat{\eta} = \frac{\eta}{L}$	(La = 0.3)	$\hat{k}_p \propto \frac{u_*}{C_s g B_{\max}}$

in this wave model is the non-dimensional peak wave number, $\hat{k}_p = k_p L$, which, from (8) and (9), can be rewritten as $\hat{k}_p \propto u_*/(C_s g B_{\max})$, suggesting $u_*/(C_s g B_{\max})$ as the only independent non-dimensional parameter arising from the surface wave model.

The surface roughness length, z_0, which represents the length scale of turbulence at the surface, transforms into the non-dimensional roughness parameter $\hat{z}_0 = z_0/L$.

All non-dimensional parameters present in this study are summarized in Tab. 3. We carefully checked that different numerical solutions indeed collapse if all non-dimensional parameters are kept constant and all variables are non-dimensionalized as in Tab. 2.

b. Non-dimensional PWP86 model

A frequently used model to describe DWL bulk parameters has been formulated by Price et al. (1986, PWP86 from here on). These authors used a vertically integrated mixed-layer model with a simple parameterization for entrainment (Pollard et al. 1973), forced, as in our study, with a constant wind stress and a surface buoyancy forcing identical to that shown in Fig. 1. Based on a scale analysis of their model equations, PWP86 suggested simple scaling relations for the DWL thickness, h, buoyancy anomaly, $\overline{b}$ (as defined in (16)), and velocity anomaly, $\overline{V} = \sqrt{(\overline{u}^2 + \overline{v}^2)}$ with

$$\overline{u} = \frac{1}{h}\int_{z_{\mathrm{ref}}}^{0} \tilde{u}\,\mathrm{d}z\,, \quad \overline{v} = \frac{1}{h}\int_{z_{\mathrm{ref}}}^{0} \tilde{v}\,\mathrm{d}z \qquad (26)$$

and $\tilde{u} = u - u_{\mathrm{ref}}$, $\tilde{v} = v - v_{\mathrm{ref}}$, all evaluated at the peak buoyancy flux (i.e., at noon). Converted to the notation used in our study, and expressed in non-dimensional form, these scaling relations can be written as:

$$\hat{h} = \frac{h}{L} = a_1 \cdot R^{-1/2} F(\hat{f}) \, , \tag{27}$$

$$\hat{\overline{b}} = \frac{\overline{b}\, u_*}{B_{\max}} = a_2 \cdot R^{-1/2} F(\hat{f})^{-1} \, , \tag{28}$$

$$\hat{\overline{V}} = \frac{\overline{V}}{u_*} = a_3 \cdot R^{-1/2} \, , \tag{29}$$

where a_1, a_2, and a_3 denote non-dimensional model constants, and F a non-dimensional model function accounting for the effect of rotation:

$$F(\hat{f}) = \frac{1}{\hat{f}} \left[2 - 2\cos(\hat{f}/2) \right]^{\frac{1}{2}} \, . \tag{30}$$

Note that only two of the non-dimensional parameters identified in the previous section, $R = u_*^2/(B_{\max} T_h)$ and $\hat{f}$, appear in the PWP86 model. The expressions in (27)-(29) apply only for the special case $\eta = 0$, i.e. if all short-wave radiation is absorbed at the surface. In section 5d, we will suggest a possible generalization for the case of penetrating short-wave radiation.

c. Parameter space studies

Before we tested the scaling relations by PWP86 over a wide parameter range, we performed parameter space studies for the non-dimensional parameters T_h/T_p, $B_0/B_{\max}$, $\hat{z}_0$, and $\hat{k}_p$ that are not included in the PWP86 scaling. Here, we set $\hat{\eta} = 0$ for simplicity, varied R over the physically relevant range $R = 10^{-4}$ to 10^{-2}, and individually tested the impact of the above non-dimensional parameters. For this parameter space study, we again used the closure model of H15 with the same time step and the same number of grid cells as in Section 4. However, the depth of the water column was now automatically adjusted to 10 times the DWL thickness at midday to ensure that the lower edge of the numerical domain had no significant impact on the results.

As shown in Fig. 8, we find that the non-dimensional parameters T_h/T_p, $B_0/B_{\max}$, $\hat{z}_0$, and $\hat{k}_p$ have a negligible impact on the non-dimensional DWL thickness $\hat{h}$ (and also on the other DWL bulk properties not shown here for brevity but included in Section 2 of the supplemental material). We note, however, that the parameters T_h/T_p and $B_0/B_{\max}$ may have a larger impact for longer simulation periods of several days, where they may affect the nighttime DWL reset and thus the

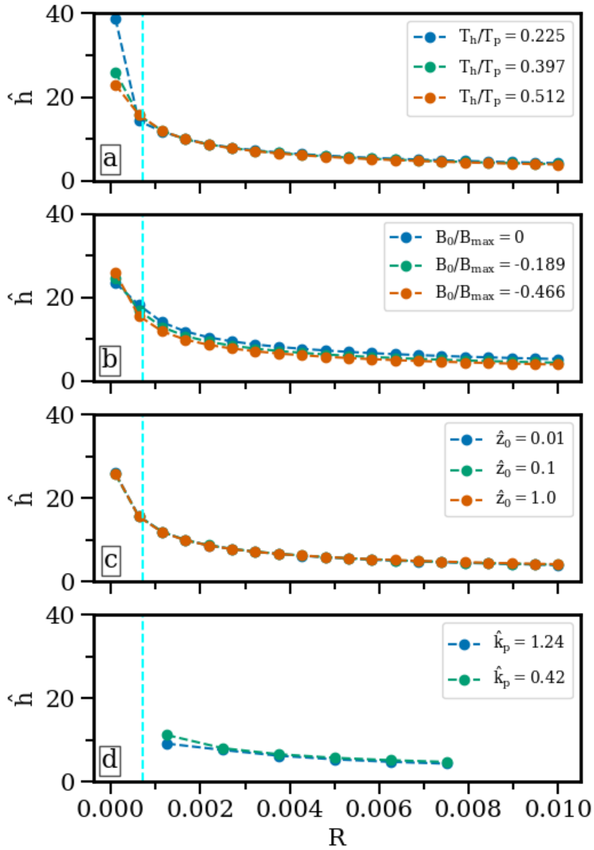

FIG. 8. Non-dimensional thickness $\hat{h}$ for constant $T_h/T_f = 0.14$ as a function of $R = u_*^2/(B_{\max} T_h)$ for different values of (a) the time scale ratio T_h/T_p, (b) the flux ratio $B_0/B_{\max}$, (c) the non-dimensional surface roughness $\hat{z}_0$, and (d) the non-dimensional peak wave number $\hat{k}_p$. All other non-dimensional parameters are kept fixed at $T_h/T_p = 0.4$, $B_0/B_{\max} = 0.466$ and $\hat{z}_0 = 0.01$, respectively. The blue dashed line shows the critical threshold for the collapse of DWL turbulence, $R = 7 \cdot 10^{-4}$, which is discussed in detail further below.

quasi-periodic evolution of the surface layer structure. Similarly, the peak wavenumber $\hat{k}_p$ may become relevant for non-equilibrium wave fields, especially for conditions when long-wave swell induces a larger penetration depth of the Stokes shear (Kukulka et al. 2013).

To test the scaling relations by PWP86, we performed a parameter space study using H15, consisting of 200 model runs, in which we varied R from 10^{-4} to 10^{-2} and $\hat{f}$ from 0 to 4.95 (or, equivalently, T_h/T_f from 0 to 0.79).

We especially focused on the model performance in high-latitude regions ($T_h/T_f > 0.5$), which are not well explored at the moment and for which the model assumptions of PWP86 are uncertain.

We again assume surface absorption ($\hat{\eta} = 0$), and that the daily average of the total buoyancy flux is zero ($B_0/B_{\max} = -0.466$, $T_h/T_p = 0.4$). The roughness length is set to $\hat{z}_0 = 0.01$.

In Fig. 9, we show simulation results for the non-dimensional DWL thickness, $\hat{h}$, bulk buoyancy, $\hat{\overline{b}}$, and bulk velocity $\hat{\overline{V}}$ at $t = T_p/2$, i.e. at midday. These quantities are normalized by the PWP86 scaling relations in (27), (28), and (29), respectively, to reveal the variability of the model parameters a_1, a_2, and a_3. Fig. 9 shows that the performance of the PWP86 scaling is generally excellent, except for a weakly forced regime with $R \lessapprox 7 \cdot 10^{-4}$ (weak winds and strong buoyancy forcing), where a strong variability in the PWP86 model parameters suggests that their scaling fails (blue dashed line in Fig. 9).

A more detailed analysis showed that turbulent and molecular diffusivities become comparable in this regime, and that Ri at the DWL base becomes much larger than the critical value for shear instability, indicating an absence of turbulent entrainment. It is worth noting that Hughes et al. (2020) studied this regime in more detail, based on high-resolution observations and a 1D model with a simpler turbulence closure without LT but similar radiative and atmospheric forcing parameters. From their simulations, these authors identified a critical wind speed of $U_{10} = 2$ m s^{-1} below which turbulent mixing does not occur. This is equivalent to $R = 6.6 \cdot 10^{-4}$ for the buoyancy forcing used in their study, and therefore consistent with the more generally applicable non-dimensional threshold suggested by our simulations with a more advanced turbulence model that also included Langmuir effects. Overall, this indicates that molecular effects become significant in this regime, suggesting that the Reynolds and Prandtl numbers are additional relevant non-dimensional parameters that have to be considered. As the effects of these parameters are not accounted for in any of the high-Re models used in our study, we don't investigate this regime any further here.

We determined the model constants a_1, a_2, and a_3 by calculating the mean of the PWP86-scaled model results shown in Fig. 9, excluding regions with $R < 7 \cdot 10^{-4}$. Tab. 4 shows that the revised constants suggest a more than 30% increase in the DWL thickness (and a correspondingly smaller buoyancy/temperature anomaly) compared to the original values by PWP86, which is significant for many applications. Most importantly, differences between DWL bulk parameters from our GOTM simulations and those predicted by the (revised) PWP86 model rarely exceed 10% (with largest deviations observed at large T_h/T_f) across the entire parameter range. Tab. 4 also shows

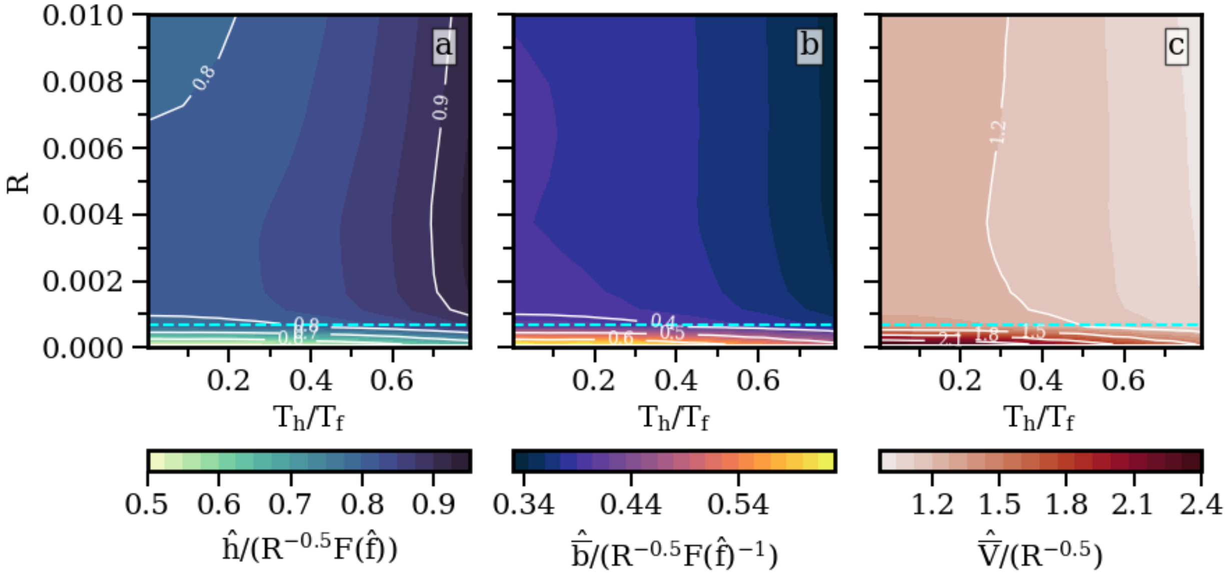

FIG. 9. DWL properties as functions of $R = u_*^2/(B_{\max} T_h)$ and $T_h/T_f = \hat{f}/(2\pi)$. Shown are midday values of (a) DWL thickness, (b) DWL bulk buoyancy, and (c) DWL bulk velocity, normalized by the PWP86 scalings in (27), (28), and (29). This implies that the results shown in (a)-(c) correspond to PWP86 model constants a_i. The blue line shows the critical value of R below which DWL turbulence does not occur.

TABLE 4. Model constants a_1, a_2 and a_3 of the PWP86 model appearing in (27)–(29). The original constants of PWP86 were converted to our notation according to: $a_1 = 0.45 \cdot 2^{1/2} = 0.63$, $a_2 = 1.5 \cdot 2^{-3/2} = 0.53$ and $a_3 = 1.5 \cdot 2^{-1/2} = 1.06$. The factor $1/2$ arises from the relation $T_h = 2P_Q$, where P_Q is the heating period in the notation of PWP86. The ranges given in the table correspond to the *maximum* deviations across the entire parameter range. Standard deviations (not shown) are considerably smaller. $t_{\max}$ is the time of maximum buoyancy anomaly. All simulations were conducted for the case $\hat{\eta} = 0$.

	$t = T_p/2$			$t = t_{\max}$	
	PWP86	with LT	without LT	with LT	without LT
a_1	0.63	0.84 ± 0.07	0.75 ± 0.1	1.08 ± 0.03	1.01 ± 0.05
a_2	0.53	0.38 ± 0.03	0.42 ± 0.05	0.56 ± 0.05	0.59 ± 0.05
a_3	1.06	1.15 ± 0.15	1.30 ± 0.2	1.3 ± 0.5	1.3 ± 0.5

that simulations without LT (not discussed in detail here) result in DWLs that are approximately 10% shallower and have a correspondingly larger buoyancy contrast.

The PWP86 scaling relations were originally proposed to predict DWL properties at the solar radiation peak ($t = T_p/2$). More relevant for many applications, including the interpretation of SST snapshots from satellite data, atmosphere-ocean coupling, and ecosystem applications, are, however, often the DWL properties at the peak of the DWL buoyancy or temperature anomaly in the afternoon. The timing of this peak cannot be determined from the PWP86 scaling. We therefore identified the (non-dimensional) time $t_{\max}/T_p$ of the maximum buoyancy anomaly numerically from our simulations.

Scaling our simulations at $t = t_{\max}$ with the expressions of PWP86 (see Section 2 of the supplemental material) suggests that the PWP86 scaling also provides an excellent representation of the DWL bulk properties during the buoyancy peak in the afternoon, provided the model coefficients a_1, a_2, and a_3 are appropriately adjusted. The values in Tab. 4 show that the DWL thickness and the buoyancy anomaly have increased by 29% and 47%, respectively, compared to midday, illustrating a strong modification of the DWL during the early afternoon. The small variability of the model coefficients in Tab. 4 supports the applicability of the PWP86 scaling also for this case, except for the diurnal jet, which shows a strong dependency on T_h/T_f especially for large values of this parameter. We attribute this to the effect of the pronounced inertial oscillations at high latitudes that are not well represented by the scaling of PWP86. The good performance of the scaling of PWP86 for the depth and bulk buoyancy at this point in time is a surprising result, as we found that the model assumption of a constant bulk Richardson number $Ri_b = \overline{b}h/\overline{V}^2 = 0.65$, which is the basis of PWP86, is not valid any more at high latitudes due to the decrease of $\overline{V}$ in the afternoon.

Fig. 10a shows that the timing of the afternoon buoyancy peak is relatively robust, generally observed between 15:00 and 16:30 with a shift towards later times for larger T_h/T_f. We attribute this shift to the suppression of entrainment of colder bottom waters due to stronger rotation effects at higher latitudes and/or a larger total buoyancy flux for larger T_h. A similar shift towards later times is observed if the short-wave absorption scale, $\hat{\eta}$, is increased (Fig. 10b,c), which results in a larger DWL thickness and therefore more time required to heat up the DWL to its maximum temperature. Overall, however, the buoyancy/temperature peak is observed in the same range 15:00-16:30 for all absorption scales we investigated.

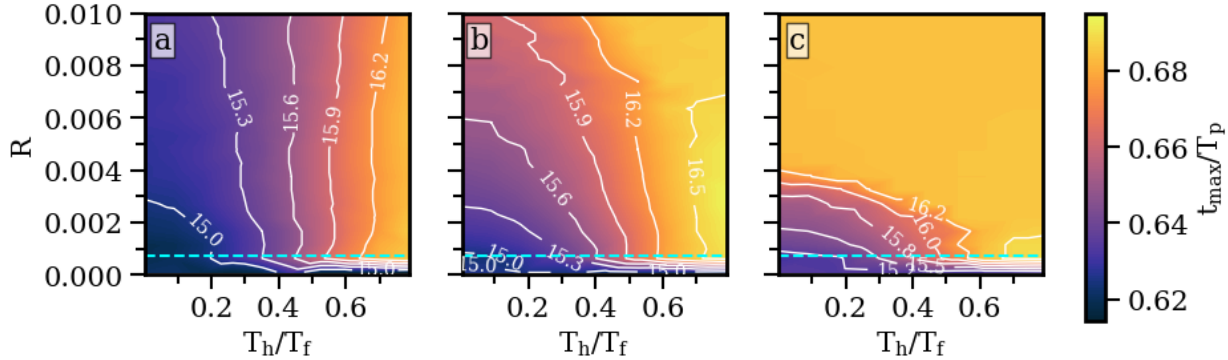

FIG. 10. Non-dimensional time $t = t_{\max}/T_p$ for varying R and T_h/T_f (the contour line labels show the time in hours of the day) for (a) $\hat{\eta} = 0$, (b) $\hat{\eta} = 2$ and (c) $\hat{\eta} = 4$.

d. Effect of penetrating short-wave radiation

To investigate the first-order impacts of penetrating short-wave radiation in the scaling of PWP86, we carried out a parameter space study similar to that shown in Fig. 9. Now, however, we varied R and $\hat{\eta}$ over the physically relevant ranges $R = 10^{-4} - 10^{-2}$ and $\hat{\eta} = 0 - 5$ at two different latitudes. We chose $T_h/T_f = 0.14$ and 0.74, corresponding to our standard tropical and high-latitude cases from Section 4, while keeping the other non-dimensional parameters constant at $T_h/T_p = 0.4$, $B_0/B_{\max} = -0.466$ and $\hat{z}_0 = 0.01$.

For the scaling, it appears physically more intuitive to relate the short-wave penetration depth η to the DWL thickness h, which yields η/h (rather than $\hat{\eta} = \eta/L$) as the key non-dimensional parameter. Fig. 11c shows that η/h always stays well below 1 for the range of $\hat{\eta}$ chosen in this study, which means that all the heat from the surface buoyancy flux is absorbed well within our definition of the DWL depth. Following the suggestion of PWP86, we parameterize the increase in thickness $\hat{h}$ due to an increase in η by multiplying the corresponding PWP86 expression in (27) with a function J that depends on $\hat{h}/\hat{\eta}$. We suggest

$$J(\hat{h}/\hat{\eta}) = \left(1 - A_\eta e^{-\hat{h}/\hat{\eta}}\right)^{-\frac{3}{2}} \tag{31}$$

where $A_\eta = 6.9$ was obtained from fitting (the original pre-factor of PWP86, $(I_b^0 - B_0)/I_b^0$, did not yield acceptable results).

TABLE 5. Model constants a_1, a_2 and a_3 at $t = T_p/2$ of the modified PWP86 scaling relations in (32)–(34), evaluated for two different latitudes.

	10°N	70°N
a_1	0.83 ± 0.14	0.83 ± 0.3
a_2	0.38 ± 0.05	0.38 ± 0.2
a_3	1.20 ± 0.3	1.20 ± 0.4

The modified PWP86 scaling that includes the effects of absorption is then given as

$$\hat{h} = a_1 \cdot R^{-1/2} F(\hat{f}) J(\hat{h}/\hat{\eta}) \,, \tag{32}$$

$$\hat{\overline{b}} = a_2 \cdot R^{-1/2} F(\hat{f})^{-1} J(\hat{h}/\hat{\eta})^{-1} \,, \tag{33}$$

$$\hat{\overline{V}} = a_3 \cdot R^{-1/2} J(\hat{h}/\hat{\eta})^{-1/3} \,, \tag{34}$$

where the model constants a_i remain unchanged for consistency with (27)–(29). As $\hat{h}$ is unknown, (32) forms an implicit non-linear equation that needs to be solved numerically. Alternatively, $\hat{h}$ appearing on the right hand side could be approximated by the original expression in (27). Tab. 5 shows the maximum deviations from the standard model constants a_i, and thus the model uncertainties, based on (32)–(34). The variability of the parameters in Tab. 5 suggests that the modified PWP86 scaling captures the effect of penetrating short-wave radiation with good accuracy for the tropical case. For the high-latitude case, however, the agreement is only moderate, suggesting the need for a more detailed analysis of the effect of penetrating radiation in high-latitude DWLs. For the according plots, please see Section 2 of the supplemental material.

Beyond its impact on the bulk DWL properties, our simulations also showed that penetrating short-wave radiation strongly affects the near-surface structure of the DWL buoyancy and velocity profiles. If $\eta > 0$, many of our simulations showed the evolution of a thin convective layer immediately below the surface. The overall effect of this additional mixing is a reduction of the surface buoyancy, similarly to the observed reduction caused by LT (see Fig. 3), suggesting that the two processes interact. In the following, we therefore investigate the combined effects of penetrating short-wave radiation and LT on the surface buoyancy b^0 and surface velocity V^0, both non-dimensionalized here by the corresponding bulk values $\overline{b}$ and $\overline{V}$.

Fig. 11a,b shows the variability of these variables as a function of the stability parameter R for a tropical $T_h/T_f = 0.14$ and different combinations of simulations with and without LT and various values of $\hat{\eta}$. As before, the other non-dimensional parameters are kept fixed at $T_h/T_p = 0.4$, $B_0/B_{\max} = 0.466$, and $\hat{z}_0 = 0.01$. While the bulk values show a change of only 10% resulting from LT (see Table 4), the surface values are influenced much more strongly by LT across the entire parameter range. The ratio $V^0/\overline{V}$ is reduced to roughly half when LT is included (Fig. 11b), which is in line with the strong reduction of the surface velocity visible in both the LES and the model of H15 in Fig. 3. The additional mixing due to LT results in a related reduction of the surface buoyancy only for the case with $\eta = 0$ (Fig. 11a), while, surprisingly, LT *increases* the surface buoyancy for the cases with $\eta > 0$. In these cases, the near-surface buoyancy is characterized by unstable thermal stratification (convection) such that the additional mixing associated with LT now brings *warmer* (less buoyant) fluid to the surface. For comparison, the linear DWL buoyancy profile assumed in Fairall et al. (1996) yields a constant $b^0/\overline{b} = 2$, while the parametric profiles of Gentemann et al. (2009) predict $b^0/\overline{b} = 3.4 - 1.3$ for increasing wind speeds (similar to our results with moderate absorption coefficient $\hat{\eta} = 2$ and LT).

6. Discussion and conclusions

Based on state-of-the-art second-moment turbulence modeling, and supported by turbulence-resolving LES, we have shown that LT strongly impacts the DWL energetics, mainly by reducing the work performed by the surface stress and partly compensating this effect by Stokes shear production. Surface buoyancy and surface velocity are strongly reduced under LT, even under weak winds, which has important implications for air-sea exchange in coupled models. With an average increase in DWL thicknesses of only around 10%, the impact of LT on DWL bulk parameters, however, turned out to be moderate. We attribute this largely to the equilibrium wave model used in our study. Although equilibrium wave fields are typical in many situations, it is worth noting that previous LES studies with monochromatic non-equilibrium waves, focusing on swell effects (Kukulka et al. 2013), have shown a stronger impact of LT on DWL properties. Under non-equilibrium wind and wave conditions and deviations from a fixed La= 0.3, the scaling coefficients that were derived in Section 5 may have to be adjusted.

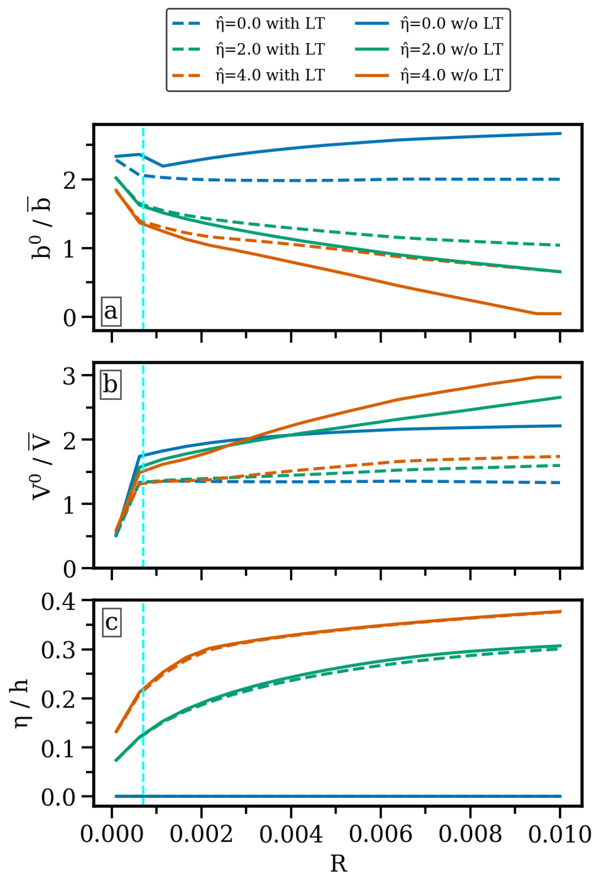

636 FIG. 11. Nondimensional DWL surface properties as functions of $R = u_*^2/(B_{\max}T_h)$ for different $\hat{\eta}$ with and without LT. Shown are midday values of (a) surface buoyancy scaled by bulk buoyancy (b) surface velocity scaled by bulk velocity and (c) absorption coefficient scaled by DWL depth. The cyan dashed line shows the critical value of R below which our DWL models are no more applicable due to molecular effects.

Dimensional analysis and the parameter space studies in Section 5 showed that the most relevant non-dimensional parameters among those compiled in Tab. 3 are the following three: the stability parameter $R = u_*^2/(B_{\max}T_h)$, the time scale ratio T_h/T_f, and the short-wave radiation absorption scale $\hat{\eta} = \eta/L$. Parameterizations that do not independently account for these parameters are unlikely to be generally applicable. E.g., the recent DWL model of Wang et al. (2023) only considers a single non-dimensional parameter, $\hat{B}_0 \propto (\hat{f}R)^{-1}$, and is therefore not applicable outside the range of latitudes and optical water properties for which it was calibrated. Similarly, Gentemann et al. (2009) suggested a parametric temperature profile with a direct dependency on the wind speed, but neglected the changes in entrainment at high latitudes. An interesting topic of future research might therefore be the development of parametric DWL profiles with a dependency on the relevant non-dimensional parameters R, T_h/T_f, and $\hat{\eta}$.

As shown in Section 5, however, the three key parameters identified above do appear independently in the frequently used DWL scaling relations of PWP86. We showed that their model reliably predicts the most important DWL bulk parameters across a wide parameter range with our different sets of revised model coefficients that include the deepening of the DWL due to LT and other aspects of our more advanced turbulence model. We suggest a simple model extension to also account for the effects of penetrating short-wave radiation, which, however only yielded good agreement with our simulations for tropical DWLs, pointing at future work for a reliable description of high-latitude DWLs. One caveat of PWP86 applies to the low-energy regime with $R = u_*^2/(B_{\max}T_h) < 7 \cdot 10^{-4}$, where molecular effects become important, and the high-Reynolds number models and parameterizations used in this study are no longer applicable. Direct Numerical Simulations appear to be the only viable approach to explore this parameter range, which is relevant especially for very thin DWLs with weak wind forcing and strong buoyancy forcing.

The excellent performance of the simple PWP86 scaling relations was a somewhat unexpected result as our parameter space also included high-latitude DWLs for which the PWP86 modeling assumption of a constant bulk Richardson number formally breaks down. In view of increasing ice-free areas at high latitudes and strong DWL temperature anomalies already observed at high latitudes (Jia et al. 2023; Eastwood et al. 2011), it is likely that the physics of these DWLs (e.g., Sutherland et al. 2016) will receive increased attention in the future.

Acknowledgments. This paper is a contribution to the project L4 (Energy-Consistent Ocean-Atmosphere Coupling) of the Collaborative Research Centre TRR 181 "Energy Transfers in Atmosphere and Ocean", funded by the German Research Foundation (DFG) under grant 274762653 to L. Umlauf. H. T. Pham and S. Sarkar are pleased to acknowledge funding by NSF grant OCE-1851390. We would like to thank Kenneth Hughes and an anonymous reviewer for their valuable contributions. Qing Li and Ramsey Harcourt provided expert input on Langmuir turbulence in GOTM.

Data availability statement. Simulations in this manuscript were carried out with a modified version of the General Ocean Turbulence Model (GOTM). The used source code is archived at `https://doi.org/10.5281/zenodo.8103884` (Klingbeil and Umlauf 2023). The LES data as well as the scripts that run GOTM and plot the figures shown in this article are archived at `https://doi.org/10.5281/zenodo.10223915` (Schmitt 2023).

APPENDIX

A1. Second-moment turbulence models

The turbulent diffusivities ν_t, ν_t^S and ν_t^b appearing in (10) and (11) are assumed to be related to the turbulent kinetic energy, k, and a turbulence length scale, l, according to

$$\nu_t = c_\mu k^{\frac{1}{2}} l \, , \quad \nu_t^S = c_\mu^S k^{\frac{1}{2}} l \, , \quad \nu_t^b = c_\mu^b k^{\frac{1}{2}} l \, . \tag{A1}$$

The stability functions c_μ, c_μ^S and c_μ^b are essential for the representation of the effects of shear, stratification, and LT on the anisotropy of turbulence.

Our analysis in Sections 4 and 5 is based on the stability functions of Harcourt (2015, H15 in the following) that constitute an improved version of an earlier model by Harcourt (2013) and are considered state of the art for the integration of LT effects in second-moment closure models. Note that the stability functions in (A1) are presented using the notation of the Generic Length Scale (GLS) framework (Umlauf and Burchard 2003). They are related to their equivalents in Mellor-Yamada notation (see H15) as $c_\mu = 2^{1/2} S_M$, $c_\mu^S = 2^{1/2} S_M^S$, and $c_\mu^b = 2^{1/2} S_H$.

H15 showed that if LT effects are included, c_μ, c_μ^S, and c_μ^b are polynomial functions of the non-dimensional time-scale ratios Nk/ε, Sk/ε, $S_c k/\varepsilon$, and $S_s k/\varepsilon$, where S_c and S_s defined in (15) represent the direct impact of Stokes shear on the stability functions that was ignored in earlier models of LT (the full expressions for the stability functions are shown in (33) of H15). One example of these earlier models is the one of Kantha and Clayson (2004, KC04 in the following) that is based on the original stability functions of Kantha and Clayson (1994), ignoring LT effects. In this case, we have $\nu_t^S = 0$, and the expressions for the shear production terms in P and P_s in (13) and (14) simplify accordingly.

Following work by KC04 and H15 on the parameterization of LT effects on the turbulent length scale, l, we compute this quantity from a modified Mellor-Yamada-type transport equation for the variable kl. These authors suggested to include an extra Stokes production term, analogous to the TKE budget in (12), in the original kl-equation of Mellor and Yamada (1982), leading to an expression of the form:

$$\frac{\partial kl}{\partial t} = D_l + l(c_{l1}P + c_{l4}P_s + c_{l3}G - c_{l2}F\varepsilon) \ , \tag{A2}$$

where the wall function $F = 1 + c_F \left(\frac{l}{\kappa L_z}\right)^2$ (here, κ is the von Kármán constant and L_z the distance from the surface) is required to reproduce the logarithmic wall layer distribution close to the surface. D_l summarizes the vertical transport terms, and c_{l1}–c_{l4} and c_F denote non-dimensional model constants (or functions) discussed in more detail below. The conversion relations between our notation and that originally used by KC04 and H15 are summarized in Tab. A1.

The dissipation rate ε follows from the cascading relation

$$\varepsilon = (c_\mu^0)^3 \frac{k^{3/2}}{l} \ , \tag{A3}$$

with c_μ^0 denoting the value of c_μ in the logarithmic wall layer (Umlauf and Burchard 2005).

As an alternative to the transport equation for kl in (A2), we also computed some of the solutions based on the k-ω model by Umlauf et al. (2003), solving (12) combined with an equation of the form

$$\frac{\partial \omega}{\partial t} = D_\omega + \frac{\omega}{k}\left(c_{\omega 1}P + c_{\omega 4}P_s + c_{\omega 3}G - c_{\omega 2}\varepsilon\right) \ , \tag{A4}$$

where ω denotes an inverse turbulence time scale defined as

$$\omega = (c_\mu^0)^{-4} \varepsilon k^{-1} \, . \tag{A5}$$

Similar to (A2), the transport equation for ω in (A4) includes a Stokes production term recently suggested by Yu et al. (2022) to account for LT effects. D_ω denotes again the turbulent transport terms, and $c_{\omega 1}$–$c_{\omega 4}$ are non-dimensional model constants (see Tab. A1).

The transport terms D_k, D_l, and D_ω appearing in (12), (A2), and (A4), respectively, are modeled by down-gradient expressions:

$$D_k = \frac{\partial}{\partial z}\left(\nu_t^k \frac{\partial k}{\partial z}\right) , \quad D_l = \frac{\partial}{\partial z}\left(\nu_t^l \frac{\partial kl}{\partial z}\right) , \quad D_\omega = \frac{\partial}{\partial z}\left(\nu_t^\omega \frac{\partial \omega}{\partial z}\right) , \tag{A6}$$

where $\nu_t^k = c_\mu^k k^{\frac{1}{2}} l$, $\nu_t^l = c_\mu^l k^{\frac{1}{2}} l$ and $\nu_t^\omega = c_\mu^\omega k^{\frac{1}{2}} l$, are turbulent diffusivities, and c_μ^k, c_μ^l, and c_μ^ω the corresponding stability functions.

The model parameters c_{l1} and c_{l2}, and similarly $c_{\omega 1}$ and $c_{\omega 2}$ for the k-ω model (all compiled in Tab. A1) are well constrained by classical data for unstratified shear layers and decaying turbulence (e.g., Umlauf and Burchard 2003). The parameters c_{l3} and $c_{\omega 3}$ determine the entrainment rate in stratified turbulent boundary layers. Their values follow from a condition on the so-scalled steady-state Richardson number, $Ri_{st} = 0.23$, corresponding to the value of the Richardson number Ri in the entrainment layer at the base of the turbulent surface layer (Umlauf and Burchard 2005). Note that $c_{l3} = 2.4$ is close to the value $c_{l3} = 2.5$ used by H15. We also follow the suggestion by H15 to limit the vertical length scale by the Ozmidov scale, $L_O = (\varepsilon N^{-3})^{1/2}$. Likewise, we use $E_4 = 1.33(1 + 0.5\mathrm{La}^{-2})^{1/3} = 2.9$ with a Langmuir number of $\mathrm{La} = 0.3$ to account for the modified near-surface slope of the turbulent length scale due to LT. For our simulations without LT effects, this expression reduces to the traditional value $E_4 = 1.33$.

The most important model parameters in (A2) and (A4) in the context of LT are those multiplying the Stokes shear production terms, respectively. For the kl-equation, we adopt H15's value $E_6 = 6$, corresponding to $c_{l4} = 3$ in GLS notation. Note that this value is close to the revised $E_6 = 7.2$ obtained from comparison to field measurements (see Kantha et al. 2010) of KC04. For the k-ω model, we follow Yu et al. (2022) and choose $c_{\omega 4} = 0.15$.

TABLE A1. Non-dimensional model constants as in (12), (A2) and (A4).

GLS notation		KC04 and H15 notation		ω	
c_{l1}	0.9	$E_1 = 2c_1$	1.8	$c_{\omega 1}$	0.55
c_{l2}	0.5	$E_2 = 2c_2$	1.0	$c_{\omega 2}$	0.83
c_{l3}	2.4	$E_3 = 2c_3$	4.8	$c_{\omega 3^-}$	-0.52
c_{l4}	3.0	$E_6 = 2c_4$	6.0	$c_{\omega 4}$	0.15
c_F	1.45	$E_4 = 2c_F$	2.9	-	-
c_μ^k	0.28	$S_q = 2^{-1/2} c_\mu^k$	0.2*	†	
c_μ^l	0.28	$S_l = 2^{-1/2} c_\mu^l$	0.2*	†	
c_μ^0	0.55	$B_1 = 2^{3/2} (c_\mu^0)^{-3}$	16.6	c_μ^0	0.55

*: Only for KC04. For H15, these change according to (A7)

†: $c_\mu^{k,\omega} = c_\mu / \sigma_{k,\omega}$ with $\sigma_{k,\omega} = 2.0$

For H15, the stability functions for the transport terms in (A6) are defined as

$$S_q = S_l = [0.2^2 + (0.41 S_H)^2]^{1/2} , \tag{A7}$$

to account for the enhanced transport due to LT (here, S_H is the stability function for the turbulent diffusivity of heat, c_μ^b in our notation). In the original model of Kantha and Clayson (1994) without LT effects, and in KC04, the stability functions reduce to constants. KC04 suggested $S_l/S_q = 3.7$ but, similar to Harcourt (2013), we find that $S_l = S_q = 0.2$ is more in line with the LES results. For the k-ω model, the stability functions c_μ^k and c_μ^ω are chosen proportional to c_μ (see Umlauf et al. 2003) with constant proportionality factors expressed in terms of the turbulent Schmidt numbers σ_k and σ_ω (see Tab. A1).

Finally, we use the following boundary conditions for (12) and (A2):

$$k = \frac{u^{*2}}{(c_\mu^0)^2} \quad \text{at} \quad z = 0 \quad , \qquad \frac{\partial k}{\partial z} = 0 \quad \text{at} \quad z = -\infty \tag{A8}$$

$$l = \kappa z_0 \quad \text{at} \quad z = 0 \quad , \qquad \frac{\partial kl}{\partial z} = 0 \quad \text{at} \quad z = -\infty \, , \tag{A9}$$

where z_0 is the surface roughness length. For the upper boundary, these boundary conditions follow from the classical law-of-the-wall relations (see Umlauf and Burchard 2005). Please note that we do not consider the injection of TKE by breaking surface waves. A more detailed discussion of how z_0 affects the class of models used in our study with and without wave breaking can be found in Umlauf and Burchard (2003).

A2. Large Eddy Simulations

The three-dimensional Craik-Leibovich equations for the grid-filtered Eulerian velocity components, U_i, and buoyancy, B, are numerically solved in the LES as follows:

$$\begin{aligned}
\frac{\partial U_i}{\partial x_i} &= 0 \\
\frac{DU_i}{Dt} &= \epsilon_{ijk}(U_j + u_j^s) f_k + \epsilon_{ijk} u_j^s \omega_k - \frac{\partial \Pi}{\partial x_i} + b\delta_{i3} + \nu \frac{\partial^2 U_i}{\partial x_j^2} - \frac{\partial \tau_{ij}^{sgs}}{\partial x_j} \\
\frac{DB}{Dt} &= -u_j^s \frac{\partial B}{\partial x_j} + \nu^b \frac{\partial^2 B}{\partial x_j^2} - \frac{\partial Q_j^{sgs}}{\partial x_j} + \frac{\partial I_b}{\partial z} \, .
\end{aligned} \tag{A10}$$

Here, ω_k is the vorticity and $D/Dt = \partial/\partial t + U_j \partial/\partial x_j$. The generalized pressure (Π) is defined as

$$\Pi = \frac{p}{\rho_0} + \frac{2e}{3} + \frac{1}{2}\left[|U_i + u_i^s|^2 - |U_i|^2 \right],$$

where p is the dynamic pressure and e is the subgrid turbulent kinetic energy. A Poisson equation derived by taking the divergence of the momentum equation in (A10) is solved to obtain the modified pressure ($p + 2e/3$) using a multigrid method.

To compute the subgrid stresses $\tau_{ij}^{sgs} = -\nu_{sgs}(\partial U_i/\partial x_j + \partial U_j/\partial x_i)$ in (A10), we use the subgrid parameterization in Ducros et al. (1996) to obtain the subgrid viscosity ν_{sgs}:

$$\nu_{sgs} = 0.0014 C_K^{-3/2} \Delta_f [\tilde{F}_2^{(3)}]^{1/2} \tag{A11}$$

where the Kolmogorov constant C_K is set to be 0.5 and Δ_f is the grid filter width. Here, $\tilde{F}_2^{(3)}$ is the second-order structure filtered function obtained after applying a high-pass filter in the horizontal directions to eliminate the larger scales of the field as follows. First, the high-pass filter is applied three times sequentially to the LES velocity to obtain an explicitly filtered velocity, denoted by $\tilde{U}$. Then, the second-order structure function $\tilde{F}_2^{(3)}$ is calculated from the filtered velocity field $\tilde{U}$ using the four neighboring points in the horizontal directions as follows:

$$\left(\tilde{F}_2^{(3)}\right)_{i,j,k} = \frac{1}{4}\left[\| \tilde{U}_{i+1,j,k} - \tilde{U}_{i,j,k} \|^2 + \| \tilde{U}_{i-1,j,k} - \tilde{U}_{i,j,k} \|^2 \ \ldots \right. \\ \left. + \| \tilde{U}_{i,j+1,k} - \tilde{U}_{i,j,k} \|^2 + \| \tilde{U}_{i,j-1,k} - \tilde{U}_{i,j,k} \|^2 \right]. \tag{A12}$$

The subscripts i, j, and k in the equation above indicate the grid indices in the x, y, and z, directions, respectively. A unity subgrid Prandtl number is used to calculate the subgrid buoyancy flux Q_j^{sgs}. Further details of the numerical method used in the LES can be found in VanDine et al. (2020) and Pham et al. (2023).

The computational domain is a rectangular box with dimensions of $64 \times 64 \times 72$ m in the x, y, and z directions, respectively, using a grid size of 256^3. The grid is uniform in the horizontal directions with a spacing of 0.25 m. We use a fine vertical grid spacing of 0.05 m at the surface, and mildly stretch the grid at a rate of 3% in the region below.

The LES is initialized with zero velocity and a fixed buoyancy value throughout the domain. Periodicity is enforced at the horizontal boundaries. The wind stress components, τ_x^0 and τ_y^0, and the surface buoyancy flux, B_0, are applied at the top surface as implemented in the second-moment turbulence modeling approach. Homogeneous Neumann boundary conditions (zero gradients) are used at the bottom boundary for the horizontal velocity components and buoyancy while the vertical velocity component is set to zero at the bottom. A sponge layer is set up in the bottom 20 m to absorb possible fluctuations excited by turbulence in the surface layer.

References

Bellenger, H., and J.-P. Duvel, 2009: An Analysis of Tropical Ocean Diurnal Warm Layers. *J. Clim.*, **22 (13)**, 3629–3646, https://doi.org/10.1175/2008JCLI2598.1.

Brilouet, P.-E., J.-L. Redelsperger, M.-N. Bouin, F. Couvreux, and C. Lebeaupin Brossier, 2021: A case-study of the coupled ocean–atmosphere response to an oceanic diurnal warm layer. *Q. J. R. Meteorol. Soc.*, **147 (736)**, 2008–2032, https://doi.org/10.1002/qj.4007.

Ducros, F., P. Comte, and M. Lesieur, 1996: Large-eddy simulation of transition to turbulence in a boundary layer developing spatially over a flat plate. *Journal of Fluid Mechanics*, **326**, 1–36, https://doi.org/10.1017/S0022112096008221.

Eastwood, S., P. Le Borgne, S. Péré, and D. Poulter, 2011: Diurnal variability in sea surface temperature in the Arctic. *Remote Sensing of Environment*, **115 (10)**, 2594–2602, https://doi.org/10.1016/j.rse.2011.05.015.

Fairall, C. W., E. F. Bradley, D. P. Rogers, J. B. Edson, and G. S. Young, 1996: Bulk parameterization of air-sea fluxes for Tropical Ocean-Global Atmosphere Coupled-Ocean Atmosphere Response Experiment. *J. Geophys. Res. Oceans*, **101 (C2)**, 3747–3764, https://doi.org/10.1029/95JC03205.

Gentemann, C. L., P. J. Minnett, and B. Ward, 2009: Profiles of ocean surface heating (POSH): A new model of upper ocean diurnal warming. *Journal of Geophysical Research: Oceans*, **114 (C7)**, https://doi.org/10.1029/2008JC004825.

Harcourt, R. R., 2013: A Second-Moment Closure Model of Langmuir Turbulence. *J. Phys. Oceanogr.*, **43 (4)**, 673–697, https://doi.org/10.1175/JPO-D-12-0105.1.

Harcourt, R. R., 2015: An Improved Second-Moment Closure Model of Langmuir Turbulence. *J. Phys. Oceanogr.*, **45 (1)**, 84–103, https://doi.org/10.1175/JPO-D-14-0046.1.

Hughes, K. G., J. N. Moum, and E. L. Shroyer, 2020: Evolution of the Velocity Structure in the Diurnal Warm Layer. *J. Phys. Oceanogr.*, **50 (3)**, 615–631, https://doi.org/10.1175/JPO-D-19-0207.1.

Hughes, K. G., J. N. Moum, E. L. Shroyer, and W. D. Smyth, 2021: Stratified Shear Instabilities in Diurnal Warm Layers. *J. Phys. Oceanogr.*, **51 (8)**, 2583–2598, https://doi.org/10.1175/JPO-D-20-0300.1.

Jia, C., P. J. Minnett, and B. Luo, 2023: Significant Diurnal Warming Events Observed by Saildrone at High Latitudes. *Journal of Geophysical Research: Oceans*, **128 (1)**, e2022JC019 368, https://doi.org/10.1029/2022JC019368.

Johnson, L., B. Fox-Kemper, Q. Li, H. T. Pham, and S. Sarkar, 2023: A Finite-Time Ensemble Method for Mixed Layer Model Comparison. *Journal of Physical Oceanography*, **53 (9)**, 2211–2230, https://doi.org/10.1175/JPO-D-22-0107.1.

Kahru, M., J.-M. Leppanen, and O. Rud, 1993: Cyanobacterial blooms cause heating of the sea surface. *Marine Ecology Progress Series*, **101 (1/2)**, 1–7, 24840590.

Kantha, L., H. U. Lass, and H. Prandke, 2010: A note on Stokes production of turbulence kinetic energy in the oceanic mixed layer: Observations in the Baltic Sea. *Ocean Dynamics*, **60 (1)**, 171–180, https://doi.org/10.1007/s10236-009-0257-7.

Kantha, L. H., and A. C. Clayson, 2004: On the effect of surface gravity waves on mixing in the oceanic mixed layer. *Ocean Modelling*, **6 (2)**, 101–124, https://doi.org/10.1016/S1463-5003(02)00062-8.

Kantha, L. H., and C. A. Clayson, 1994: An improved mixed layer model for geophysical applications. *J. Geophys. Res. Oceans*, **99 (C12)**, 25 235–25 266, https://doi.org/10.1029/94JC02257.

Kawai, Y., and A. Wada, 2007: Diurnal sea surface temperature variation and its impact on the atmosphere and ocean: A review. *J Oceanogr*, **63 (5)**, 721–744, https://doi.org/10.1007/s10872-007-0063-0.

Klingbeil, K., and L. Umlauf, 2023: GOTM source code with langmuir turbulence closure. Zenodo, URL https://doi.org/10.5281/zenodo.8103884.

Kukulka, T., A. J. Plueddemann, and P. P. Sullivan, 2013: Inhibited upper ocean restratification in nonequilibrium swell conditions. *Geophys. Res. Lett.*, **40 (14)**, 3672–3676, https://doi.org/10.1002/grl.50708.

Large, W. G., and J. M. Caron, 2015: Diurnal cycling of sea surface temperature, salinity, and current in the CESM coupled climate model. *J. Geophys. Res. Oceans*, **120 (5)**, 3711–3729, https://doi.org/10.1002/2014JC010691.

Li, Q., and B. Fox-Kemper, 2020: Anisotropy of Langmuir turbulence and the Langmuir-enhanced mixed layer entrainment. *Phys. Review. Fluids*, **5 (013803)**, 1–20, https://doi.org/10.1103/PhysRevFluids.5.013803.

Li, Q., B. Fox-Kemper, Ø. Breivik, and A. Webb, 2017: Statistical models of global Langmuir mixing. *Ocean Modelling*, **113**, 95–114, https://doi.org/10.1016/j.ocemod.2017.03.016.

Matthews, A. J., D. B. Baranowski, K. J. Heywood, P. J. Flatau, and S. Schmidtko, 2014: The Surface Diurnal Warm Layer in the Indian Ocean during CINDY/DYNAMO. *J. Clim.*, **27 (24)**, 9101–9122, https://doi.org/10.1175/JCLI-D-14-00222.1.

McWilliams, J. C., P. P. Sullivan, and C.-H. Moeng, 1997: Langmuir turbulence in the ocean. *J. Fluid Mech.*, **334**, 1–30, https://doi.org/10.1017/S0022112096004375.

Mellor, G. L., and T. Yamada, 1982: Development of a turbulence closure model for geophysical fluid problems. *Rev. Geophys.*, **20 (4)**, 851–875, https://doi.org/10.1029/RG020i004p00851.

Moulin, A. J., J. N. Moum, and E. L. Shroyer, 2018: Evolution of Turbulence in the Diurnal Warm Layer. *J. Phys. Oceanogr.*, **48 (2)**, 383–396, https://doi.org/10.1175/JPO-D-17-0170.1.

Pham, H. T., S. Sarkar, L. Johnson, B. Fox-Kemper, P. P. Sullivan, and Q. Li, 2023: Multi-Scale Temporal Variability of Turbulent Mixing During a Monsoon Intra-Seasonal Oscillation in the Bay of Bengal: An LES Study. *Journal of Geophysical Research: Oceans*, **128 (1)**, e2022JC018 959, https://doi.org/10.1029/2022JC018959.

Phillips, O. M., 1958: The equilibrium range in the spectrum of wind-generated waves. *Journal of Fluid Mechanics*, **4 (4)**, 426–434, https://doi.org/10.1017/S0022112058000550.

Pollard, R. T., P. B. Rhines, and R. O. Thompson, 1973: The deepening of the wind-mixed layer. *Geophys. Astrophys. Fluid Dyn.*, **4 (1)**, 381–404.

Price, J. F., R. A. Weller, and R. Pinkel, 1986: Diurnal cycling: Observations and models of the upper ocean response to diurnal heating, cooling, and wind mixing. *J. Geophys. Res. Oceans*, **91 (C7)**, 8411–8427, https://doi.org/10.1029/JC091iC07p08411.

Sarkar, S., and H. T. Pham, 2019: Turbulence and Thermal Structure in the Upper Ocean: Turbulence-Resolving Simulations. *Flow Turbulence Combust*, **103 (4)**, 985–1009, https://doi.org/10.1007/s10494-019-00065-5.

Schmitt, M., 2023: Scripts for 'Diurnal Warm Layers in the Ocean: Energetics, Non-dimensional Scaling, and Parameterization'. Zenodo, URL https://doi.org/10.5281/zenodo.10223915.

Stull, R., 1988: *An Introduction to Boundary Layer Meteorology*. Atmospheric and Oceanographic Sciences Library, Springer Netherlands, URL https://books.google.com.au/books?id=eRRz9RNvNOkC.

Sutherland, G., L. Marié, G. Reverdin, K. H. Christensen, G. Broström, and B. Ward, 2016: Enhanced Turbulence Associated with the Diurnal Jet in the Ocean Surface Boundary Layer. *J. Phys. Oceanogr.*, **46 (10)**, 3051–3067, https://doi.org/10.1175/JPO-D-15-0172.1.

Suzuki, N., and B. Fox-Kemper, 2016: Understanding Stokes forces in the wave-averaged equations. *Journal of Geophysical Research: Oceans*, **121 (5)**, 3579–3596, https://doi.org/10.1002/2015JC011566.

Umlauf, L., and H. Burchard, 2003: A generic length-scale equation for geophysical turbulence models. *J. Mar. Res.*, **61 (2)**, 235–265, https://doi.org/10.1357/002224003322005087.

Umlauf, L., and H. Burchard, 2005: Second-order turbulence closure models for geophysical boundary layers. A review of recent work. *Continental Shelf Research*, **25 (7)**, 795–827, https://doi.org/10.1016/j.csr.2004.08.004.

Umlauf, L., H. Burchard, and K. Bolding, 2005: GOTM - Scientic Documentation : Version 3.2. **63**, 279, https://doi.org/10.12754/MSR-2005-0063.

Umlauf, L., H. Burchard, and K. Hutter, 2003: Extending the k–ω turbulence model towards oceanic applications. *Ocean Modelling*, **5 (3)**, 195–218, https://doi.org/10.1016/S1463-5003(02)00039-2.

VanDine, A., H. T. Pham, and S. Sarkar, 2020: Investigation of les models for a stratified shear layer. *Computers and Fluids*, **198**, 104 405.

Wang, X., T. Kukulka, J. T. Farrar, A. J. Plueddemann, and S. F. Zippel, 2023: Langmuir Turbulence Controls on Observed Diurnal Warm Layer Depths. *Geophysical Research Letters*, **50 (10)**, e2023GL103 231, https://doi.org/10.1029/2023GL103231.

Wijesekera, H. W., D. W. Wang, and E. Jarosz, 2020: Dynamics of the Diurnal Warm Layer: Surface Jet, High-Frequency Internal Waves, and Mixing. *J. Phys. Oceanogr.*, **50 (7)**, 2053–2070, https://doi.org/10.1175/JPO-D-19-0285.1.

Yu, C., J. Song, S. Li, and S. Li, 2022: On an Improved Second-Moment Closure Model for Langmuir Turbulence Conditions and Its Application. *J. Geophys. Res. Oceans*, **127 (5)**, e2021JC018 217, https://doi.org/10.1029/2021JC018217.